Surface & Coatings Technology 503 (2025) 132012

Contents lists available at ScienceDirect

Surface & Coatings Technology

journal homepage: www.elsevier.com/locate/surfcoat

Hybrid chondroitin sulfate-tailored phosphate coatings for improved corrosion and wear resistance of WE43 magnesium alloy

Lei Yang [a,b], Yanbin Zhao [a,b,d], Yumeng Dong [a,b], Juyi Yang [a,b], Shuyi Wang [a,b], Cheng Wang [a,b], Jing Bai [a,b,c], Feng Xue [a,b], Paul K. Chu [d], Chenglin Chu [a,b,*]

[a] School of Materials Science and Engineering, Southeast University, Nanjing 211189, China
[b] Jiangsu Key Laboratory for Advanced Metallic Materials, Southeast University, Nanjing 211189, China
[c] Institute of Medical Devices (Suzhou), Southeast University, Suzhou 215163, China
[d] Department of Physics, Department of Materials Science and Engineering, Department of Biomedical Engineering, City University of Hong Kong, Hong Kong, China

ARTICLE INFO

Keywords:
Biodegradable magnesium alloy
Hybrid coating
Hydrothermal treatment
Corrosion resistance
Wear resistance

ABSTRACT

Biodegradable magnesium (Mg) alloys are useful for bone screws, but their anti-corrosion and anti-wear coatings properties may be inadequate *in vivo*. Herein, a hybrid $MgKPO_4{\cdot}6H_2O$ (MKP)/chondroitin sulfate A (CSA) coating with a uniform and crack-free morphology is prepared on the WE43 Mg alloy by a hydrothermal treatment. The corrosion current density (4.219×10^{-6} A/cm^2) of the MKP-CSA coating is an order of magnitude smaller than that of the bare Mg, and the hydrogen evolution rate (0.0005 mL·cm^{-2}·h^{-1}) and corrosion rate (0.47 ± 0.01 mm/y) improve significantly as well. Tribologically, the coating shows an average friction coefficient of 0.239 ± 0.019 and a wear rate of 17.94×10^{-5} mm^3/N·m, which are 35.6% and 46.4% less than those of the Mg alloy. Our study demonstrates that the complex formed by chelation of CSA with Mg^{2+} provides *in situ* nucleation sites for MKP. The enhanced corrosion resistance of the hybrid coating stems from the optimized structure, and the wear resistance can be attributed to the higher adhesion strength and hardness, and the combination of the relatively hard inorganic material of MKP and soft polymer of CSA. The results reveal a new strategy to fabricate hybrid inorganic-organic coatings on biodegradable Mg alloys with excellent corrosion and wear resistance for clinical applications.

1. Introduction

Magnesium (Mg) alloys are suitable for temporary orthopedic implants due to their biodegradability, biocompatibility, as well as elastic modulus close to that of human bone [1–4]. However, the downside of Mg is the excessive corrosion rate [5,6]. Bare Mg tends to corrode quickly in the physiological environment [7,8], thus losing the mechanical integrity before tissues can fully heal. Furthermore, corrosion of Mg generates hydrogen that can lead to tissue inflammation [9,10]. The degradation rate of Mg-based biomaterials can be regulated by surface modification such as micro-arc oxidation, chemical conversion coatings, physical vapor deposition, and layer-by-layer assembly [11,12]. Chemical conversion coatings have the advantages of environmentally friendliness and easy preparation. Phosphate conversion coatings composed of calcium phosphate (Ca–P) and magnesium phosphate (Mg–P) can enhance the corrosion resistance and biocompatibility of Mg alloys. However, unavoidable cracks in these coatings compromise their efficacy as a physical barrier. In the early stage, Mg corrosion generates Mg^{2+} leading to the formation of $Mg(OH)_2$ and competitive adsorption with Ca^{2+} from the solution [4]. Because there are few adsorption sites for Ca–P crystal nucleation on bare Mg, it is challenging to prepare a dense Ca–P coating with high adhesion strength [13].

To address these issues, Mg–P coatings have been proposed. Since Mg contributes to the formation of Mg–P, the bonding between the coating and substrate can be improved. Mg-based phosphate has been used in minimally invasive bone grafting surgery because of its good biocompatibility, reliable mechanical properties, and osteogenic capabilities [14–16]. For example, Tan et al. [17] have prepared the $NH_4MgPO_4{\cdot}6H_2O$ cement with anti-inflammatory, immunomodulatory, and osteogenic effects. However, it is easy to generate ammonia, consequently causing tissue damage and inflammation of surrounding tissues. Replacing the raw material ($NH_4H_2PO_4$) with KH_2PO_4 not only avoids the toxic effects of ammonium ions, but also helps to maintain the

* Corresponding author at: School of Materials Science and Engineering, Southeast University, Nanjing 211189, China.
E-mail address: clchu@seu.edu.cn (C. Chu).

https://doi.org/10.1016/j.surfcoat.2025.132012
Received 18 November 2024; Received in revised form 28 February 2025; Accepted 4 March 2025
Available online 5 March 2025
0257-8972/© 2025 Elsevier B.V. All rights are reserved, including those for text and data mining, AI training, and similar technologies.

electrolyte balance inside and outside the cell via potassium ion [18,19]. Ren et al. [20] have developed a nano amorphous Mg–P and PLA composite coating on AZ31 with good corrosion resistance and biocompatibility. Hence, if inorganic Mg–P is combined with organic polymers, the effects can be better than those offered by a single inorganic coating.

Chondroitin sulfate (CS) is a glycosaminoglycan found in the non-collagenous extracellular matrix of human bone [21]. It has the effects of cartilage regeneration, anti-inflammation, and anti-oxidation [22–24]. Sulfonic and carboxylate groups in CS can react strongly with positively charged groups [25], such as Mg^{2+}, through ionic interactions to form covalent bonds and provide *in situ* nucleation sites for Mg–P. Besides, the friction between orthopedic implants and bone during the turnover process can result in various levels of wear [26,27]. The majority of coatings with low wear resistance can be worn during implantation [28], and strong wear resistance is equally crucial. Herein, MKP and MKP-CSA coatings are prepared on the WE43 Mg alloy hydrothermally, and characterized systematically. The results reveal that the optimal coating has enhanced corrosion and wear resistance.

2. Experimental details

2.1. Materials

The as-extruded WE43 Mg alloy was purchased from Suzhou Rongqian Rare Metal Product Co., Ltd. and cut into specimens with dimensions of 20 mm × 20 mm × 5 mm. Chondroitin sulfate A (CSA, 98%) was obtained from Shanghai Yuanye Bio-Technology Co., Ltd., and sodium hydroxide (NaOH), phosphoric acid (H_3PO_4), and potassium phosphate monobasic (KH_2PO_4) were obtained from Xilong Science Co., Ltd. Magnesium oxide (MgO) was bought from Shanghai Macklin Biochemical Co., Ltd. All the reagents were used without purification.

Ultrapure (UP) water with a resistivity of 18 MΩ·cm (25 °C) was obtained from the Milli-Q water system. The Mg substrate was ground with SiC paper up to 2000 grids, immersed in a 5.0 M NaOH solution for 0.5 h, flushed with water, and dried at 110 °C for 2 h to provide the initial negative layer for subsequent deposition.

2.2. Fabrication of the MKP-CSA coating

As shown in Fig. 1, the hybrid $MgKPO_4{\cdot}6H_2O$ (MKP)/chondroitin sulfate-A (CSA) coating was fabricated on WE43 by a hydrothermal treatment. The 2 mg/mL CSA solution was prepared and stirred at 60 °C for 0.5 h, followed by the addition of 17 mg/mL KH_2PO_4 and 5 mg/mL MgO. The mixture was stirred at 60 °C for 0.5 h, and the pH was adjusted to 8.0 by H_3PO_4. Then, the sample and solution were put in an autoclave and treated at 120 °C for 4 h. Afterward, the sample was taken out, washed with water, and dried at 37 °C for 12 h. The preparation of the MKP inorganic coating was similar, except that the CSA solution was omitted.

2.3. Materials characterization

The surface morphology of the samples was examined by scanning electron microscopy (SEM, Nova Nano SEM450, USA) at 20 kV, and the composition was determined by energy-dispersive X-ray spectroscopy (EDS). X-ray diffraction (XRD, Bruker D8-Discover, Germany) was performed with a Cu K_α X-ray source (1.5418 Å) from $2\theta = 10–90°$ in steps of 0.15°/s. Fourier transform infrared spectroscopy (FT-IR, Thermo Scientific Nicolet iS10, USA) was conducted in the range between 4000 and 500 cm^{-1} with a resolution of 0.4 cm^{-1}, and X-ray photoelectron spectroscopy (XPS, Thermo Scientific K Alpha, USA) was performed to determine the chemical composition and phase of the coatings.

2.4. Corrosion assessment

2.4.1. Electrochemical evaluation

The Princeton electrochemical workstation (Ametek PARSTAT 3000A-DX) with a three-electrode configuration was employed to determine the electrochemical properties of the WE43 substrate as well as MKP and MKP-CSA coatings. The saturated calomel electrode and Pt sheet were the reference and counter electrodes, while the sample with an exposed area of 1 cm^2 was the working electrode. Electrochemical impedance spectroscopy (EIS) was conducted with an AC amplitude of 10 mV AC between 100 kHz and 100 mHz to ensure the reliability and repeatability of the data. Potentiodynamic polarization (PDP) was carried out at a scanning rate of 1 mV/s *vs* SCE from −2.5 to −1.0 V, and the relatively complete anode polarization and cathode polarization curves can be obtained. The self-corrosion potential (E_{corr}, V/SCE) and corrosion current density (i_{corr}, A/cm^2) were acquired by Tafel extrapolation. The above process was carried out in Hank's balanced salt solution (HBSS) [29], and the data were analyzed by the Versastudio and ZSimpWin software.

2.4.2. Hydrogen evolution

The burette-funnel apparatus was used to monitor the hydrogen release [30]. The sample was immersed in HBSS for 7 days at 37.5 ± 0.1 °C. The hydrogen evolution rate (v_H, mL·cm^{-2}·h^{-1}) was derived by Eq. (1) [31]:

$$v_H = \frac{V}{st} \tag{1}$$

where V is the volume of hydrogen released (mL), s is the exposed surface area (cm^2), and t is the immersion time (h), respectively.

2.4.3. Mass loss

The sample was taken out after immersion for 1, 3, and 7 days in HBSS, dipped into a chromate acid solution (200 g/L of CrO_3 solution saturated with 10 g/L of $AgNO_3$) to remove the corrosion products, and cleaned ultrasonically for 20 min. The corrosion rate (*CR*, mm/y) was calculated by Eq. (2) [32,33]:

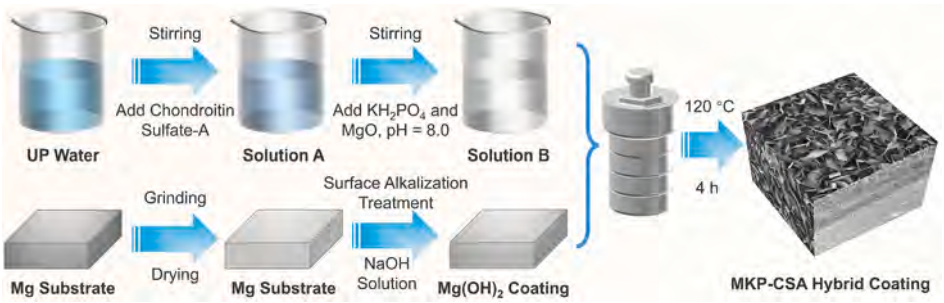

Fig. 1. Schematic diagram of the fabrication process of the MKP-CSA coating.

$$CR = \frac{8.76 \times 10^4 \times \Delta m}{A \times t \times \rho} \quad (2)$$

where Δm is the mass loss (g), A is the exposed surface area (cm^2), t is the total immersion time (h), and ρ is the alloy density (1.84 g/cm^3), respectively. The ratio of HBSS to surface area was 100 mL/cm^2, and the pH variation was recorded during the mass loss test. To improve the statistics, a triplicate analysis was performed. SEM, EDS, XRD, FT-IR, and XPS were applied to characterize the sample after immersion.

2.5. Adhesion strength and microhardness assessment

The adhesion strength of the coating was measured according to the standard ISO 2409-2020 Paints and Varnishes-Cross-Cut Test [33,34]. Microhardness tests were done by Micro Vickers hardness tester (FM-700) under 100 gf load and 10 s holding time. Each indentation point in the measurement was 0.2 mm away from the other points, and at least quintuplicate analysis was performed to improve the statistics.

2.6. Tribology assessment

The friction and wear testing machine (Bruker (CETR) UMT-2) was used to determine the friction and wear properties at room temperature. A GCr15 bearing steel ball with a diameter of 3 mm was the friction partner, and the WE43 substrate and two coated samples (MKP and MKP-CSA) were the grinding materials. The friction load was 5 N, the friction stroke was circular motion with a radius of 3 mm, the friction rate was 120 r/min, and the friction time was 12 min. The morphology of the sample after the experiment was examined on the friction profilometer (ADE Phase-Shift MicroXAM-3D), and the volume of the coating loss (V) was monitored by the laser confocal microscope and profilometer. The wear rate (K) was estimated by Eq. (3) [35]:

$$K = \frac{V}{F \times S} \quad (3)$$

where the F and S represent the friction load (N) and sliding distance (m), respectively.

3. Results

3.1. Materials characterization

Fig. 2 shows that the MKP and MKP-CSA coatings have a flaky and stacked morphology. The MKP coating in Fig. 2b–c has a compact structure, whereas some of the flakes gather into spheres, as shown in Fig. 2a. The hybrid chondroitin sulfate-tailored MKP-CSA coating has less MKP reunion than the bare MKP coating (Fig. 2d–f). The optimized microstructure can be attributed to the nucleation of negatively charged groups in CSA. According to EDS (Fig. 2g–i), the Mg/P atomic ratios of the MKP and MKP-CSA coatings are 1.24 and 1.13, respectively, as a result of different degrees of Mg corrosion during coating preparation.

Fig. 3 presents the SEM cross-sectional morphologies of the MKP and MKP-CSA coatings together with EDS maps and coating thickness. There are tiny holes in the MKP coating (Fig. 3a), revealing that the stacking of the flaky MKP along the C-axis is not as uniform as expected. On the contrary, the MKP-CSA coating has a compact structure in line with the surface morphology (Fig. 3b), and the rectangular shape attests to the homogeneity of the hybrid coating. The coating thickness can be derived from the cross-section image and EDS line scan (Fig. 3c, e). As shown in Fig. 3d, the thickness of the MKP-CSA coating (7.51 ± 0.28 μm) is larger

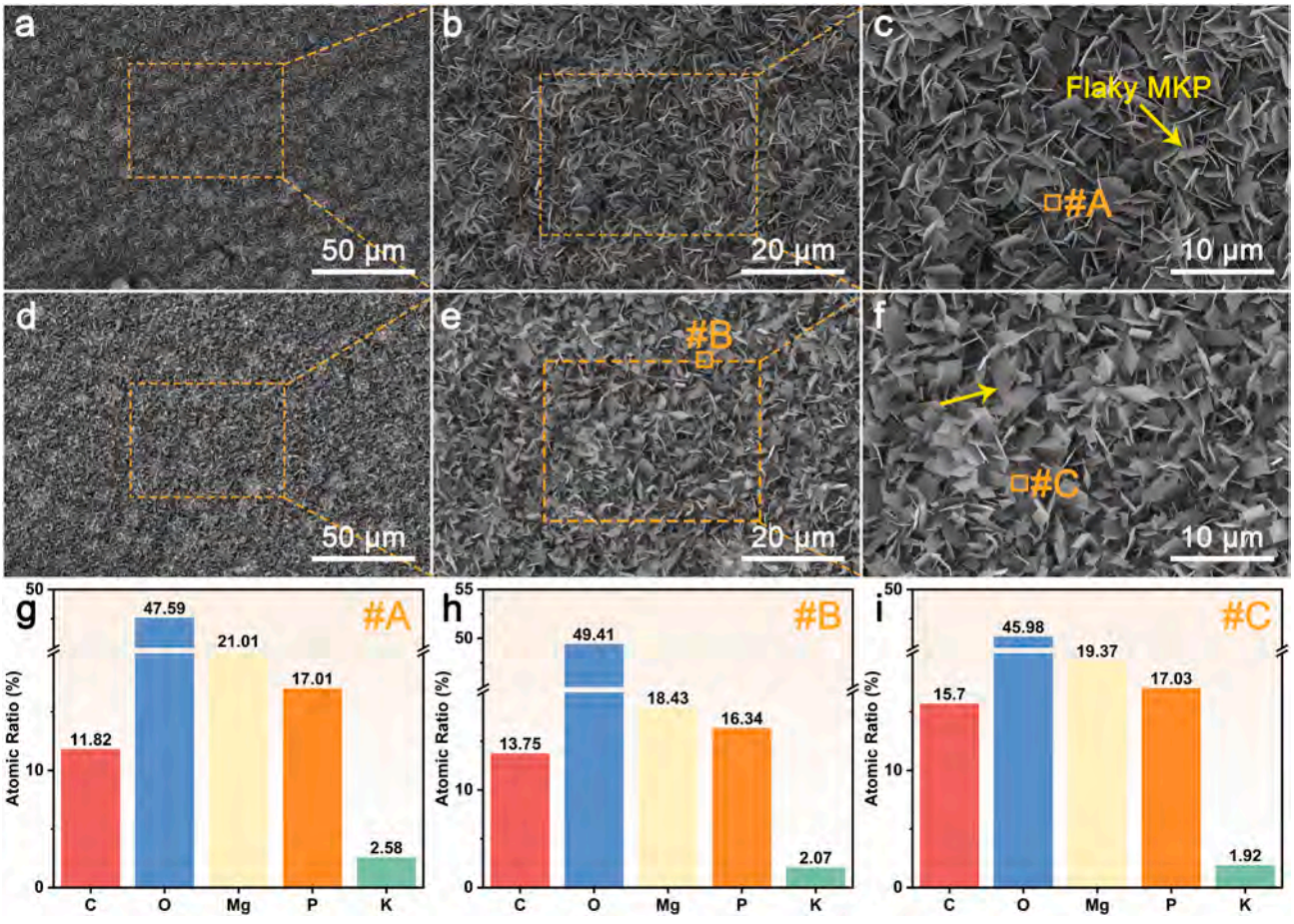

Fig. 2. SEM surface morphologies of (a–c) MKP and (d–f) MKP-CSA coatings; (g–i) EDS results.

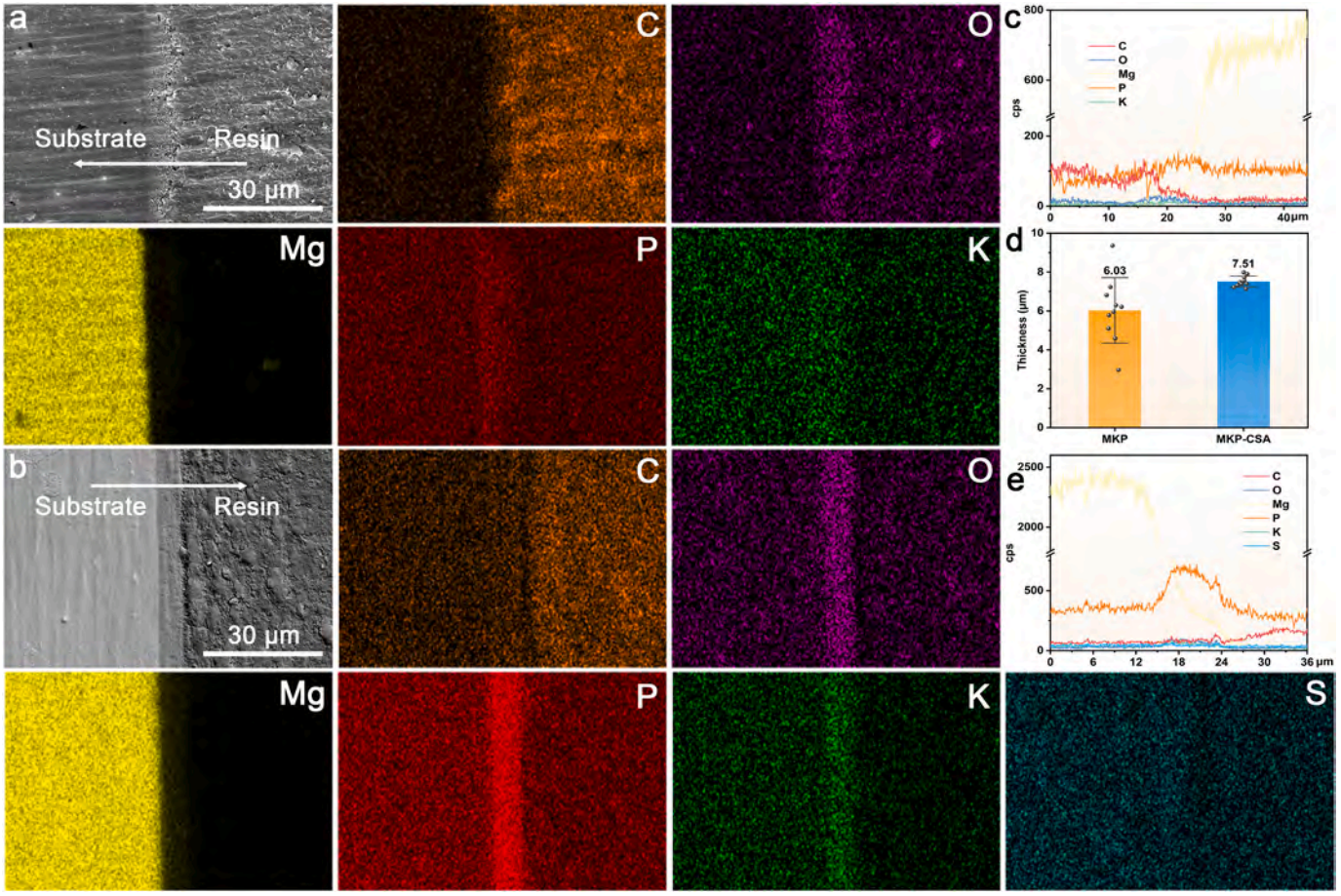

Fig. 3. SEM cross-sectional morphologies of (a) MKP and (b) MKP-CSA coatings together with EDS elemental maps; (c, e) EDS line scans and (d) coating thickness.

than that of MKP coating (6.03 ± 1.69 μm), indicating that CSA contributes to MKP growth by providing nucleation sites. According to the smaller variance of MKP-CSA coating thickness, the hybrid coating is more uniform. In addition, both the MKP and MKP-CSA coatings adhere tightly to the substrate, showing no defects such as cracks or shedding.

The XRD, FT-IR, and XPS spectra are presented in Fig. 4. As shown in Fig. 4a, the primary ingredients in the MKP and MKP-CSA coatings are $MgKPO_4{\cdot}6H_2O$ (K-struvite) and $Mg_3(PO_4)_2{\cdot}5H_2O$, further demonstrating that the inclusion of CSA will not form new inorganic phases. Different chemical bonds or functional groups are shown in Fig. 4(b1). The peaks at 3410 and 1652 cm^{-1} can be assigned to O—H stretching in H_2O and O—H bending, respectively. The tensile and bending absorption peaks at 1072, 773, and 600 cm^{-1} arise from PO_4^{3-}, confirming the formation of MKP on the substrate. The details of the functional groups of the MKP-CSA coating are shown in Fig. 4(b2). The absorption peaks at 1637, 1107, 1042, and 1015 cm^{-1} correspond to C═O, S═O, and C-O-C stretching vibrations, respectively, typical of CSA in the MKP-CSA coating [23,24]. The FT-IR spectrum of the MKP-CSA coating is generally similar to that of the MKP coating, indicating that the incorporation of CSA does not alter the chemical structure of MKP.

The survey XPS spectra (Fig. 4c) of the MKP and MKP-CSA coatings show the presence of Mg, O, K, C, P, and S, consistent with XRD and FT-IR results, with Mg, O, K, and P originating from MKP and the majority of S element from CSA. The results show that MKP is formed on the substrate, and CSA combines nicely with MKP in the hybrid coating. The high-resolution XPS spectra of C 1*s*, O 1*s*, Mg 1*s*, P 2*p*, K 2*p*, and S 2*p* are depicted in Fig. 4d. The C 1*s* spectrum of MKP coating in Fig. 4d(I) exhibits peaks at 288.50, 287.01, 286.37, and 284.79 eV corresponding to C—O, O=C-OH, C—H, and C—C groups, respectively. Interestingly, the C 1*s* spectrum of the MKP coating included peaks at 288.57, 286.08, and 284.78 eV, representing C—O, C═O, and C—C groups, respectively, while the MKP coating shows peaks at 288.57, 286.08, and 284.78 eV representing C—O, C═O, and C—C, respectively. The MKP coating inevitably contains some C upon exposure to air [36]. Fig. 4d(II–V) shows the presence of O, Mg, P, and K, and the S 2*p* spectrum shows peaks at 169.48 and 165.53 eV for S═O and S—O, confirming the existence of CSA (Fig. 4d(VI)).

3.2. Electrochemical properties

According to the PDP curves (Fig. 5a), E_{corr} and i_{corr} can be derived by the Tafel extrapolation method, as shown in Table 1. Since E_{corr} (WE43 (−1.743 V/SCE) < MKP (−1.690 V/SCE) < MKP-CSA (−1.532 V/SCE)), the MKP-CSA coating enhances the thermodynamic stability during corrosion. It is noted that the corrosion resistance cannot be reliably determined by thermodynamic parameters (E_{corr}) alone, and kinetic factors (i_{corr}) should be considered. The smaller the value of i_{corr}, the better the corrosion resistance of the coating [19]. The i_{corr} values of both coatings (9.430×10^{-6} and 4.219×10^{-6} A/cm^2) are one order of magnitude less than that of the substrate (2.489×10^{-5} A/cm^2). Besides, the MKP-CSA coating exhibited the smallest i_{corr}, indicating good corrosion protection of the Mg substrate.

As shown in the Nyquist plots (Fig. 5b), the high-frequency region is governed by the electrode reaction kinetics (charge transfer process), whereas the low-frequency region is associated with the diffusion of reactants or electrode reaction products [37]. Compared to the substrate, the larger capacitive arc radii of both coatings indicate better corrosion resistance, while the MKP-CSA coating shows a larger radius. Equivalent circuits (ECs) are devised to match the EIS results, as shown in Fig. 5e–f, and the fitted parameters are listed in Table 2, where R_s, R_c,

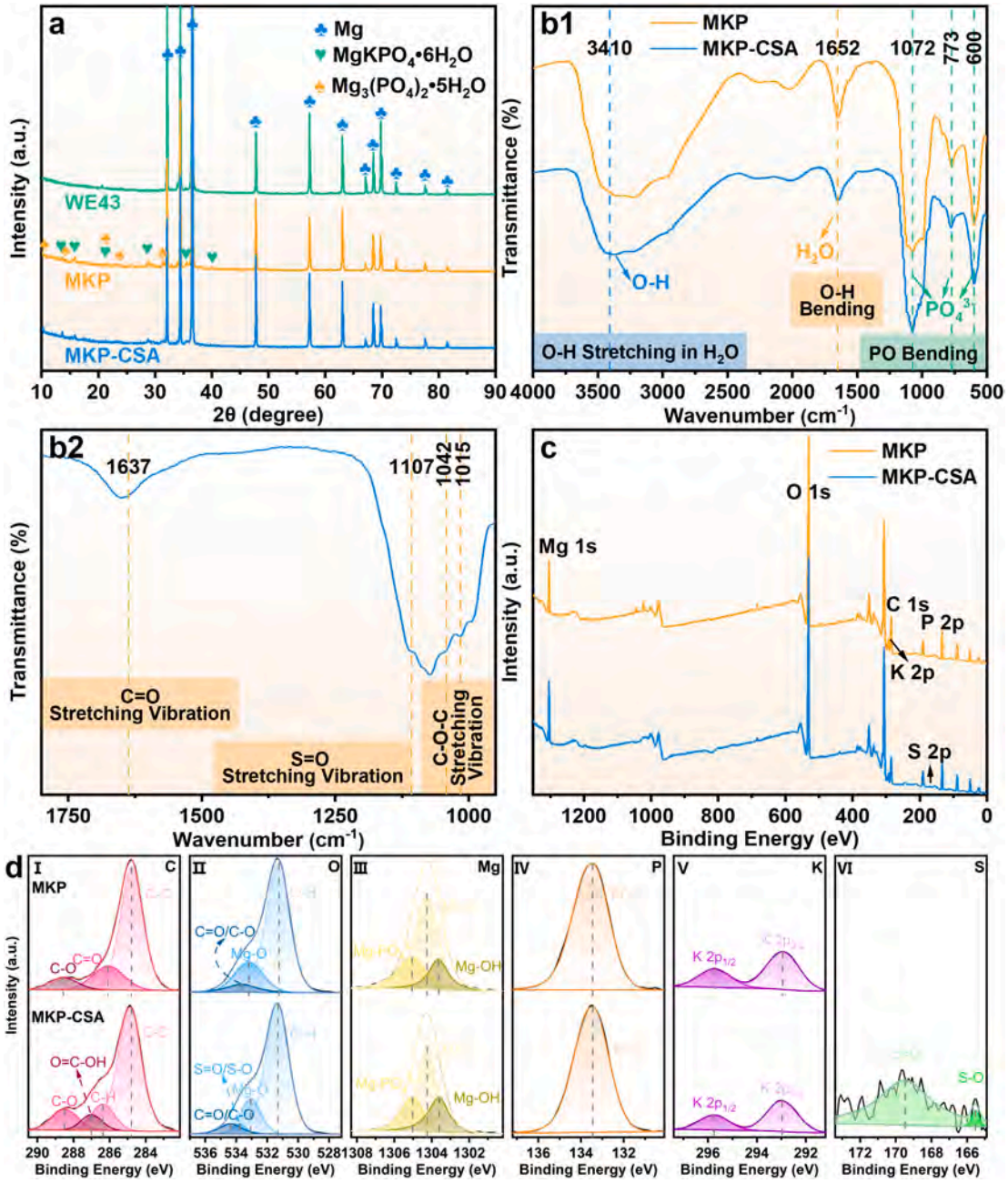

Fig. 4. XRD patterns of (a) Mg substrate, MKP coating, and MKP-CSA coating; (b1) FT-IR spectra and (b2) magnified FT-IR spectrum of the MKP-CSA coating; (c) XPS survey spectra of both coatings and (d) high-resolution XPS spectra of C 1*s*, O 1*s*, Mg 1*s*, P 2*p*, K 2*p*, and S 2*p*.

and R_{ct} denote the solution resistance, coating resistance, and charge transfer resistance, respectively. For coated samples, R_c values can be used to evaluate the anti-corrosive performance of coatings, and the greater the values, the more effective the barrier effect against corrosive species. Based on this, the hybrid CSA-tailored coating shows better barrier effect than MKP coating.

Typically, a larger R_{ct} suggests a smaller corrosion rate [38]. By applying the MKP coating, R_{ct} increases from 210.90 to 1264.30 $\Omega \cdot cm^2$, while the hybrid coating reaches 1736.13 $\Omega \cdot cm^2$. This improvement confirms the exceptional corrosion resistance. The constant phase angle element (CPE, $Y_{CPE}(\omega) = 1/Z_{CPE} = Q_a(j\omega)^n$) [33] is used to obtain better fitting results, acting as an ideal capacitor when $n = 1$ and as a pure resistor when $n = 0$. Based on the Bode plots, a large $|Z|$ at the low frequency of 0.1 Hz ($|Z|_{0.1\ Hz}$) reflects the optimal corrosion resistance. $|Z|_{0.1\ Hz}$ of the MKP-CSA coating is the largest (Fig. 5c), indicative of good corrosion resistance. The higher and wider Bode plots of the phase angle also demonstrate the superior anti-corrosive capability of the MKP-CSA coating (Fig. 5d). Analysis of the EIS data shows clearly that both coatings provide effective corrosion protection, while the hybrid coating has better effects due to the more uniform surface structure.

3.3. Immersion characteristics

The *in vitro* degradation behavior and phase analysis of the different samples immersed in HBSS for 7 days are summarized in Fig. 6. The hydrogen evolution rate (HER, v_H) after immersion for 156 h is determined (Fig. 6a), and the pH fluctuation is also monitored (Fig. 6b). After showing a large v_H at the beginning of immersion, the coatings tend to be stable the next day, but the WE43 Mg alloy still shows a large v_H. During subsequent immersion, the v_H of WE43 stabilizes at 0.002 $mL \cdot cm^{-2} \cdot h^{-1}$,

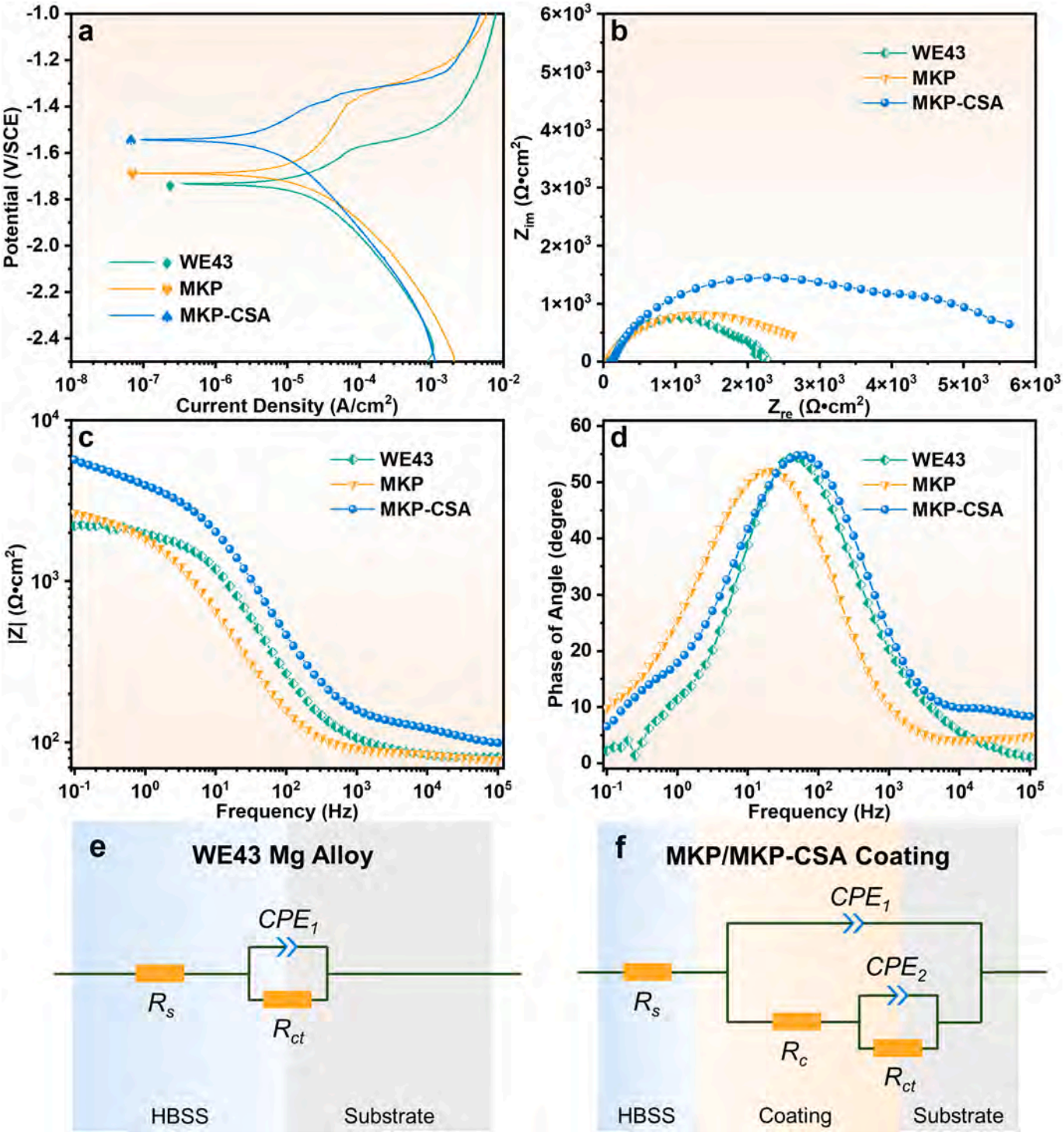

Fig. 5. Electrochemical properties of the Mg substrate, MKP and MKP-CSA coatings: (a) Potentiodynamic polarization curves; (b) Impedance spectra; (c) Bode plots; (d) Bode plots of phase angle *vs.* frequency; Equivalent circuits for (e) substrate and (f) coatings.

Table 1
E_{corr} and i_{corr} determined from the potentiodynamic polarization curves.

Samples	E_{corr} (V/SCE)	i_{corr} (A/cm^2)
WE43	−1.743	2.489×10^{-5}
MKP	−1.690	9.430×10^{-6}
MKP-CSA	−1.532	4.219×10^{-6}

which is 2 and 4 times those of the MKP (0.001 mL·cm^{-2}·h^{-1}) and MKP-CSA coatings (0.0005 mL·cm^{-2}·h^{-1}), respectively. Because the samples with and without coatings produce alkaline corrosion products, the pH of HBSS rises gradually. The pH of WE43 is larger than that of the coated samples throughout, suggesting that more corrosion products are formed.

The corrosion rates (*CR*s) of the samples in different periods (1, 3, and 7 days) are determined. The *CR* on the first day is larger than that in the later period, explaining the larger v_H and more dramatic pH

Table 2
Fitted electrochemical parameters by EIS simulation.

Samples	WE43	MKP	MKP-CSA
R_s ($\Omega \cdot cm^2$)	82.75	82.36	112.5
CPE_1 ($\Omega^{-1} \cdot cm^{-2} \cdot s^{-1}$)	2.38×10^{-5}	5.55×10^{-5}	1.66×10^{-5}
n_1	0.80	0.79	0.77
R_c ($\Omega \cdot cm^2$)	–	2178.00	4344.00
CPE_2 ($\Omega^{-1} \cdot cm^{-2} \cdot s^{-1}$)	–	0.12×10^{-4}	3.91×10^{-4}
n_2	–	0.70	0.93
R_{ct} ($\Omega \cdot cm^2$)	210.90	1264.30	1736.13
χ^2	1.62×10^{-3}	1.23×10^{-3}	4.91×10^{-3}

difference. The average *CR* during 7 days displays a declining trend: WE43 (1.91 ± 0.21 mm/y) > MKP (0.91 ± 0.05 mm/y) > MKP-CSA (0.47 ± 0.01 mm/y). Based on the v_H, pH variation, and *CR*, it can be inferred that both coatings provide certain protection to the substrate during immersion, and the hybrid coating yields the best results. The XRD patterns of the MKP and MKP-CSA coatings after immersion for 7 days show the presence of $MgKPO_4 \cdot 6H_2O$ and $Mg_3(PO_4)_2 \cdot 5H_2O$ (Fig. 6d), indicating little degradation after short-term immersion. At the same time, the characteristic peaks of $Ca_{10}(PO_4)_6(OH)_2$ (also known as hydroxyapatite, HAp) are detected. As shown in Fig. 6e, the O—H stretching, the O—H and P—O bending modes are similar to those of the MKP and MKP-CSA coatings before immersion, while the new peak at 1424 cm^{-1} corresponds to the HPO_4^{2-} and the peak at 600 cm^{-1} expands and strengthens, suggesting that both coatings promote the formation of HAp during immersion.

To determine the chemical states after immersion, XPS Mg 1*s*, O 1*s*, Ca 2*p*, K 2*p*, C 1*s*, Cl 2*p*, S 2*p*, and P 2*p* spectra are acquired from the MKP-7 d and MKP-CSA-7 d samples (Fig. 6f). The Ca 2*p* spectra suggest the formation of HAp, while the Cl 2*p* spectra show the presence of corrosive medium on the samples. Fig. 6g(I, II) shows minor changes in the binding energies of C 1*s* and O 1*s*, and the Mg 1*s*, K 2*p*, and S 2*p* spectra also do not change significantly after immersion. The P 2*p* spectra of both coatings show peaks at 134.22 and 134.20 eV corresponding to HPO_4^{2-} groups (Fig. 6g(III)) consistent with FT-IR. The Ca $2p_{3/2}$ and Ca $2p_{1/2}$ peaks also provide evidence of the formation of HAp (Fig. 6g(IV)), which provides better osteogenic ability [39,40].

Fig. 7 exhibits the macroscopic morphology of the samples at various

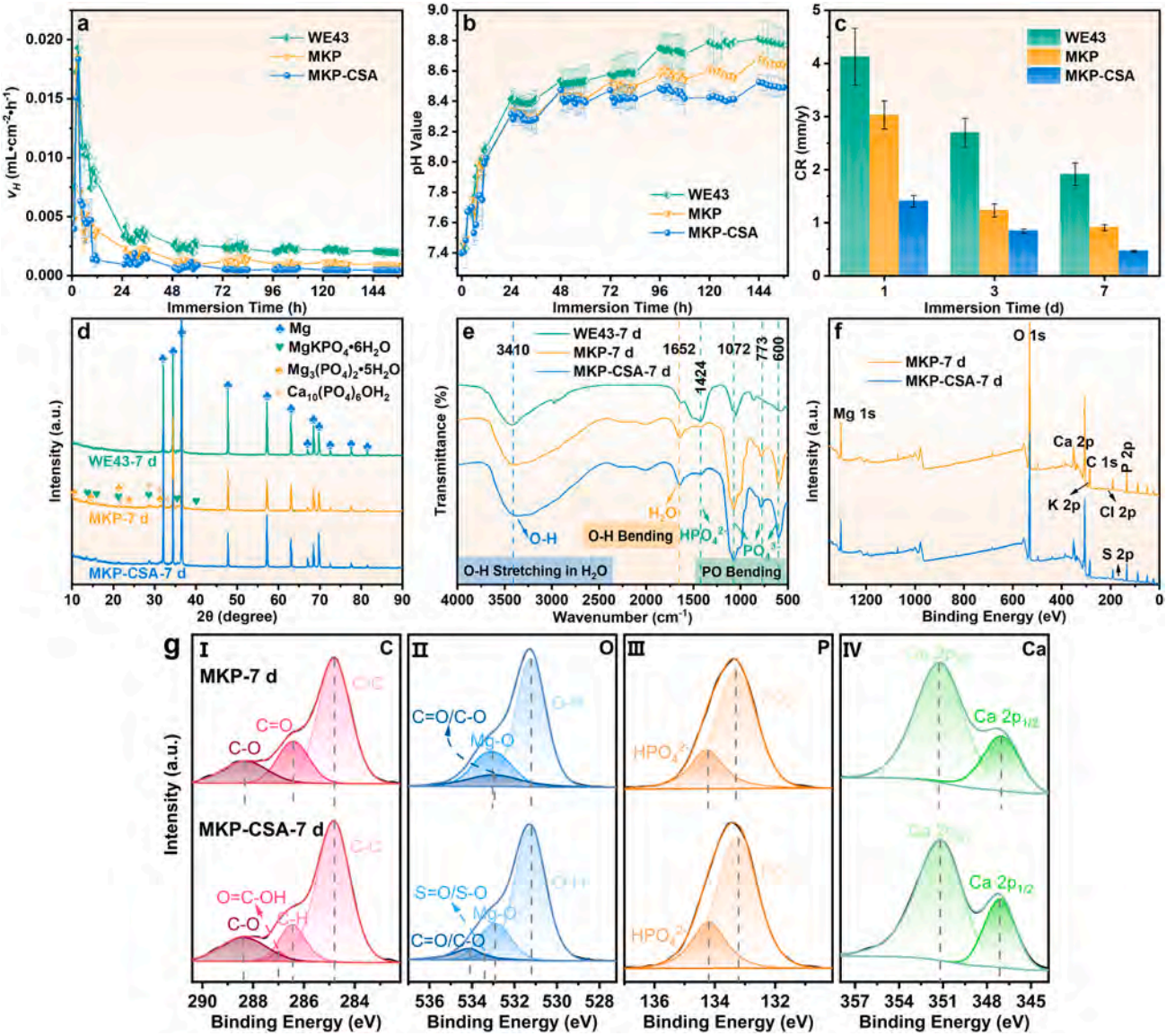

Fig. 6. Immersion results for 7 days in HBSS: (a) Hydrogen evolution rates; (b) pH variations; (c) Corrosion rates; (d) XRD patterns; (e) FT-IR spectra of the Mg substrate-7 d, MKP-7 d and MKP-CSA-7 d coatings; (f) XPS survey spectra of the MKP-7 d and MKP-CSA-7 d coatings; (g) High-resolution XPS spectra of C 1*s*, O 1*s*, P 2*p*, and Ca 2*p*.

stages (0, 1, 3, and 7 days) to assess the corrosion degree. Corrosion of the WE43 Mg alloy increases with immersion time. Comparing a1 to a4 in Fig. 7, more dark corrosion products and multiple corrosion pits emerge. The MKP coating does not change much in the initial stage (Fig. 7(b1–b3)), in spite of the appearance of several corrosion pits on the 7th day (Fig. 7(b4)). No visible flaws are found from the MKP-CSA coating after immersion (Fig. 7(c1–c4)) in line with the electrochemical results.

As shown in Fig. 8, cracks of various widths and certain corrosion products appear on WE43 (Fig. 8(a1–a3)), thus allowing the corrosion medium to penetrate to the Mg alloy. According to the surface morphologies of both coatings (Fig. 8(b2, c2)), the corrosion products mainly nucleate at the edge of the flaky MKP and morph into ellipsoids. The MKP-CSA coating maintains a suitable morphology after immersion (Fig. 8(c1–c3), while the reunion aggravates in MKP coating (Fig. 8 (b1–b3). Therefore, the closer arrangement and combination of the hybrid coating provides better stability. However, the weak combination in the MKP coating and pitting corrosion impair the bonding with the substrate, resulting in cracks and even coating delamination.

EDS shows that the corrosion products are mainly magnesium phosphate and calcium phosphate (HAp) (Fig. 8(b4, c4). The Ca/P ratios of both coatings are lower than the stoichiometric value (especially in comparison with the Mg/P ratios), showing that Ca-deficient HAp is formed on the surface. Owing to the high ionization tendency of Mg, the WE43 alloy corrodes rapidly in an aqueous, and the released Mg^{2+} replaces Ca^{2+} from HAp [4].

The cross-sectional morphologies of the samples after immersion for 7 days are monitored, as shown in Fig. 9. There are multiple deep cracks in the cross-section of WE43, and some of them extend to a deeper depth (Fig. 9a). This undoubtedly aggravates Mg corrosion and the coatings can mitigate the effect. According to the EDS maps, Ca enrichment is observed, suggesting the formation of HAp. Although no obvious defects are found from the MKP coating, tiny holes and cracks are observed in the interior (Fig. 9b), and they weaken the protective effect. Fortunately, the coating adheres to the substrate strongly. Even after immersion for 7 days in HBSS, the MKP-CSA coating retains the uniform structure and shows a compact cross-section (Fig. 9c).

3.4. Adhesion strength, microhardness and wear properties

The macro-morphologies of both coatings before and after the cross-cut tape tests are depicted in Fig. 10a–d. The MKP-CSA coating does not delaminate, indicating that CSA improves the coating-substrate adhesion. According to ASTM (American Society for Testing Materials), the adhesion strengths of the MKP and MKP-CSA coatings are Grade 1 (small pieces peeling off at the intersection of the cut with the actual damage in the grid area $\leq$ 5%) and Grade 0 (edge of the cut totally smooth and no peeling at the grid edge), respectively. Actually, the superior adhesion strength of the hybrid coating factors into the enhanced corrosion and wear resistance. The microhardness of MKP-CSA coating reaches 104.61 $\pm$ 6.59 HV (Fig. 10e), which is higher than that of substrate (87.91 $\pm$ 5.95 HV) and MKP coating (93.95 $\pm$ 5.22 HV). The addition of CSA can simultaneously improve the adhesion strength and microhardness of the coating.

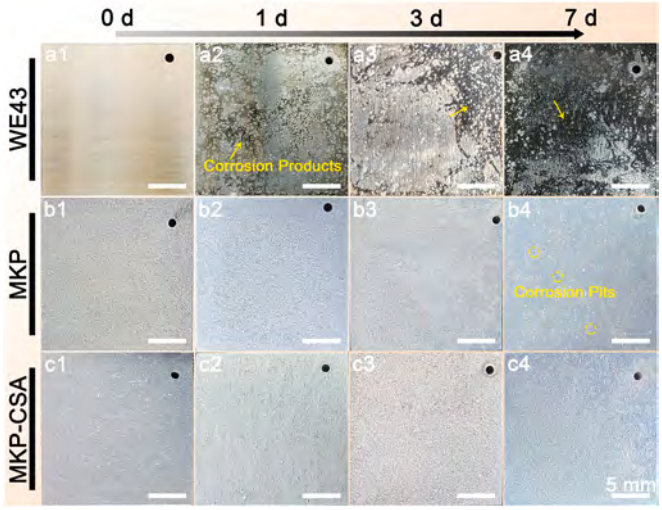

Fig. 7. Macroscopic morphologies of (a1–a4) Mg substrate, (b1–b4) MKP coating, and (c1–c4) MKP-CSA coating after immersion in HBSS for 0, 1, 3, and 7 days.

Most previous research works on Mg alloys and coatings focus on corrosion resistance and biocompatibility, but wear resistance is also crucial to clinical applications, as debris falling off from implants can compromise wound healing. Hence, the tribological characteristics of the WE43 substrate, MKP coating, and MKP-CSA coating are determined systematically, as shown in Fig. 10f–m. Fig. 10f shows how the friction coefficient varies with sliding time. With increasing sliding time, the friction coefficients of WE43 and MKP fluctuate in various ranges, indicative of some instability, while MKP-CSA stabilizes after showing some initial variations. The average friction coefficients of the WE43 Mg substrate, MKP, and MKP-CSA are 0.324 $\pm$ 0.032, 0.276 $\pm$ 0.027, and 0.239 $\pm$ 0.019, and the wear rates are 26.26, 19.47, and 17.94 (10^{-5} $mm^3/N{\cdot}m$), respectively. It is clear that the friction coefficient and wear rate of WE43 are the largest, while the MKP coating improves the wear resistance.

Fig. 10h–m shows the morphology of the wear tracks to further illustrate the tribological behavior. Some furrows and spalling pits are observed from the three-dimensional and surface wear tracks of WE43 (Fig. 10h, k). There are also several deep furrows in the center of the wear track, indicating that the wear debris cannot be discharged from the contact area in time. The debris slides relative to the contact surface of the sample under the action of the friction pair, causing serious wear. The wear track of the bare WE43 is consistent with the large friction coefficient and wear rate.

With regard to the sample coated with brittle MKP, fracture occurs during the test, leading to the formation of small particles in the three-dimensional morphology (Fig. 10i, j). The rigid and brittle particles produce micro-damage during the friction process. Nevertheless, the overall friction loss of the coatings is minimal as a result of the uniform layered structure of MKP. The more uniform flaky MKP in hybrid coating improves the adhesion strength, and the softness and good plasticity of CSA can realize certain wear reduction [22]. The enhanced wear resistance is proven by the smaller average friction coefficient and wear rate.

4. Discussion

4.1. Coating formation mechanism

As previously stated, the pH of the hydrothermal reaction solution is about 8.0, and the alkaline environment leads to the corrosion reaction (4) of the WE43 Mg substrate in the initial:

$$Mg + 2H_2O \rightarrow Mg(OH)_2 + H_2\uparrow \quad (4)$$

This reaction supplies Mg^{2+} to the solution and dissolved KH_2PO_4 releases K^+ and PO_4^{3-}, which react with MgO and Mg^{2+} to generate MKP. The chemical reactions (5–7) presented below elucidate the formation process of $MgKPO_4{\cdot}6H_2O$ and $Mg_3(PO_4)_2{\cdot}5H_2O$:

$$MgO + KH_2PO_4 + 5H_2O \rightarrow MgKPO_4{\cdot}6H_2O \quad (5)$$

$$Mg^{2+} + K^+ + PO_4^{3-} + 6H_2O \rightarrow MgKPO_4{\cdot}6H_2O \quad (6)$$

$$3Mg^{2+} + 2PO_4^{3-} + 5H_2O \rightarrow Mg_3(PO_4)_2{\cdot}5H_2O \quad (7)$$

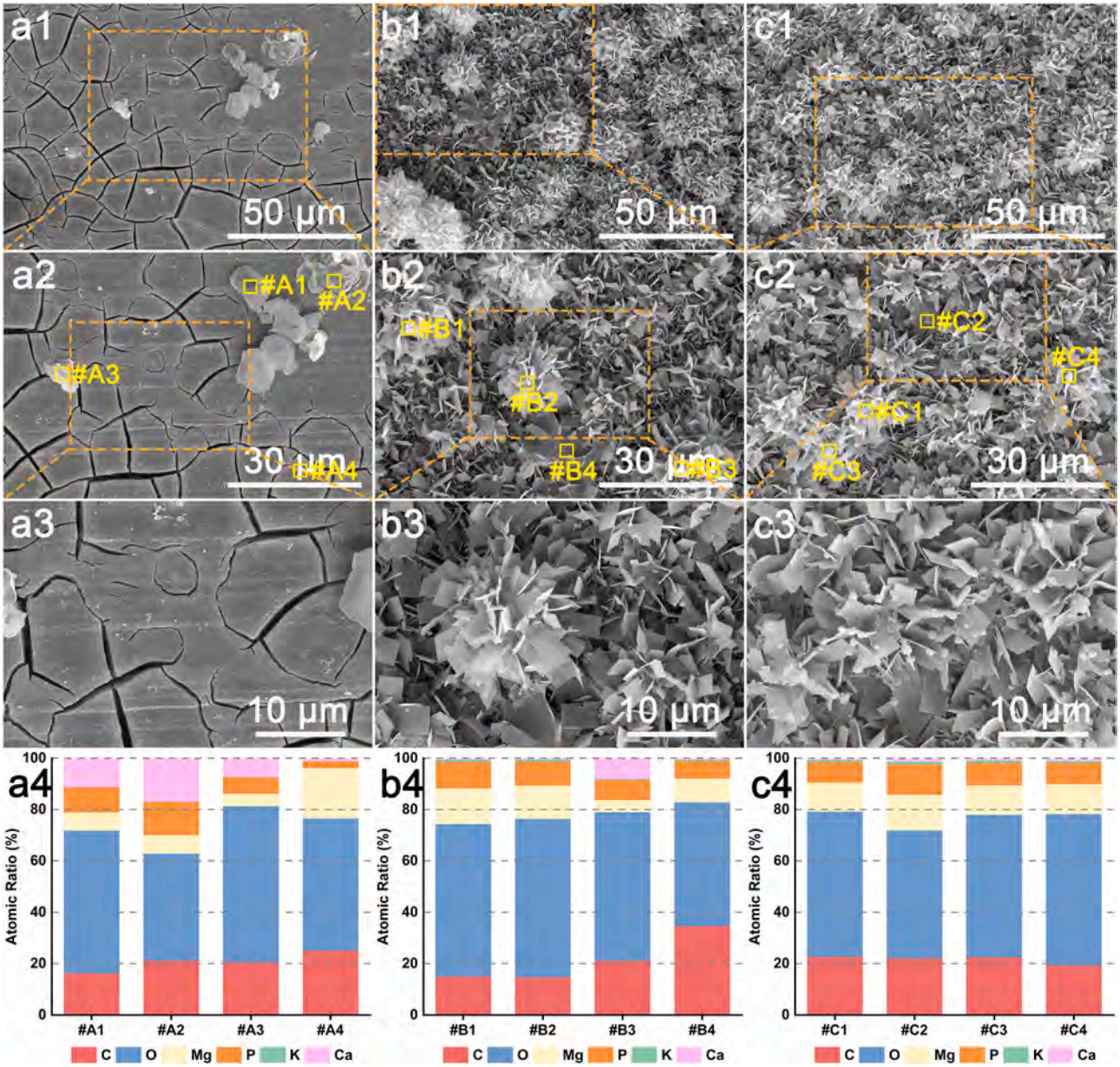

Fig. 8. Surface morphologies after immersion in HBSS for 7 days: (a1–a3) Mg substrate, (b1–b3) MKP coating, and (c1–c3) MKP-CSA coating; (a4–c4) EDS results.

During the hydrothermal reaction, dissolved KH_2PO_4 and MgO constantly release ions involved in the preceding reaction, and the continuously formed MKP precipitate consumes these ions. In the reciprocal positive feedback mechanism, MKP is deposited continuously on the substrate. The deposition of MKP is random and does not affect the homogeneity and direction of nucleation. As a result of the loose arrangement of flaky MKP and weak bonding strength, the MKP coating produced has a loose structure and weak bonding force. The bonding strength between the MKP coating and substrate is higher than that of the conventional Ca–P coating. This enhancement arises from the fact that the Mg substrate constitutes one of the reactants to improve the overall stability of the coating and the compatibility with the substrate.

In contrast, in the solution with CSA, the negatively charged sulfate group (SO^{3-}) in CSA selectively attracts positively charged ions from the environment, and PO_4^{3-} in the medium combines with Mg^{2+} and K^+ to form the hybrid *in situ* structure of MKP and CSA, as illustrated in Fig. 11. CSA offers directed nucleation sites for MKP, and facilitates the formation of a uniform and stable flaky MKP. Mg^{2+} and negatively charged sulfate groups have an attraction for neutral nucleation sites to drive the process. According to the surface and cross-sectional morphologies of the hybrid coating and the bonding force, the *in situ*-grown flaky MKP has a more uniform structure, as well as stronger bonding.

Fig. 11 explains the formation of the coating on the microscopic level. Without sufficient guidance, the deposition of flaky MKP on the substrate is random. However, stacking cannot form a uniform protective coating in general but rather forms defects such as holes which compromise the adhesion strength as well as corrosion and wear resistance. In fact, CSA chelates with Mg^{2+} to form the CSA-Mg complex to stabilize the flaky MKP and enhance the adhesion strength.

4.2. Corrosion mechanism

According to the electrochemical and *in vitro* immersion tests, the coating improves the corrosion resistance of the WE43 Mg alloy. The corrosion mechanism is proposed, as shown in Fig. 12. With regard to the substrate with the MKP coating, degradation of MKP proceeds in the initial immersion stage, as follows:

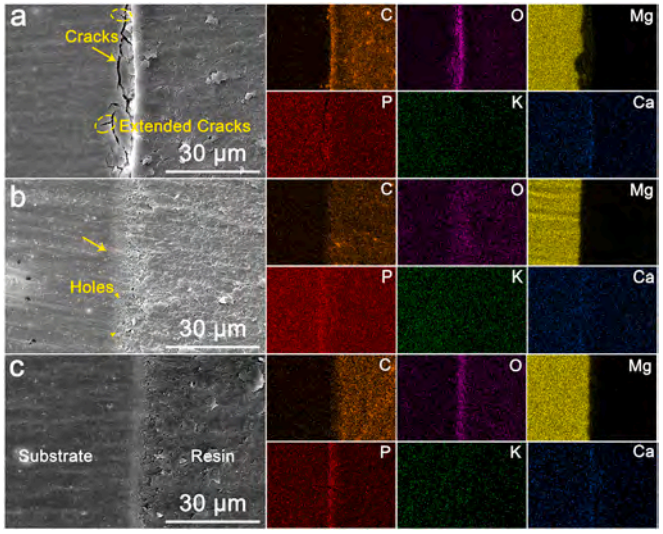

Fig. 9. Cross-sectional morphologies after immersion in HBSS for 7 days: (a) Mg substrate, (b) MKP coating, and (c) MKP-CSA coating together with the EDS maps.

$$MgKPO_4 \cdot 6H_2O \rightarrow Mg^{2+} + K^+ + PO_4^{3-} + 6H_2O \quad (8)$$

$$PO_4^{3-} + H_2O \rightarrow HPO_4^{2-} + OH^- \quad (9)$$

The products of the above reaction include Mg^{2+}, PO_4^{3-}, and OH^-, which take part in the formation of HAp:

$$10Ca^{2+} + 6PO_4^{3-} + 2OH^- \rightarrow Ca_{10}(PO_4)_6(OH)_2 \quad (10)$$

In the process, MKP in the coating degrades gradually, and HAp is deposited on the surface to provide positive feedback. The protective coating makes it difficult for corrosive species such as water molecules and Cl^- to penetrate to the substrate, resulting in controlled degradation. However, the thickness of the MKP coating varies, and the compactness and adhesion strength are not as good as those of the hybrid coating. Although the corrosion rate is nearly the same, the degradation of thinner regions brings the corrosive species closer to the substrate. After immersion, the thinner areas in the coating corrode preferentially, as shown in Fig. 12a, leading to accelerated corrosion of Mg in HBSS and the electrochemical reaction in reaction (4). This reaction can be further expressed as follows:

$$Mg \rightarrow Mg^{2+} + 2e^- \quad (11)$$

$$2H_2O + 2e^- \rightarrow 2OH^- + H_2\uparrow \quad (12)$$

The above reaction degrades Mg faster to produce $Mg(OH)_2$, raises the pH, and produces hydrogen. Corrosion can also cause coating delamination boding ill for biomedical implants. In contrast, the MKP-CSA coating retains the uniform structure following immersion. During the initial immersion stage, the MKP-CSA coating is attacked by the corrosive species, but degradation spurs the formation of corrosion

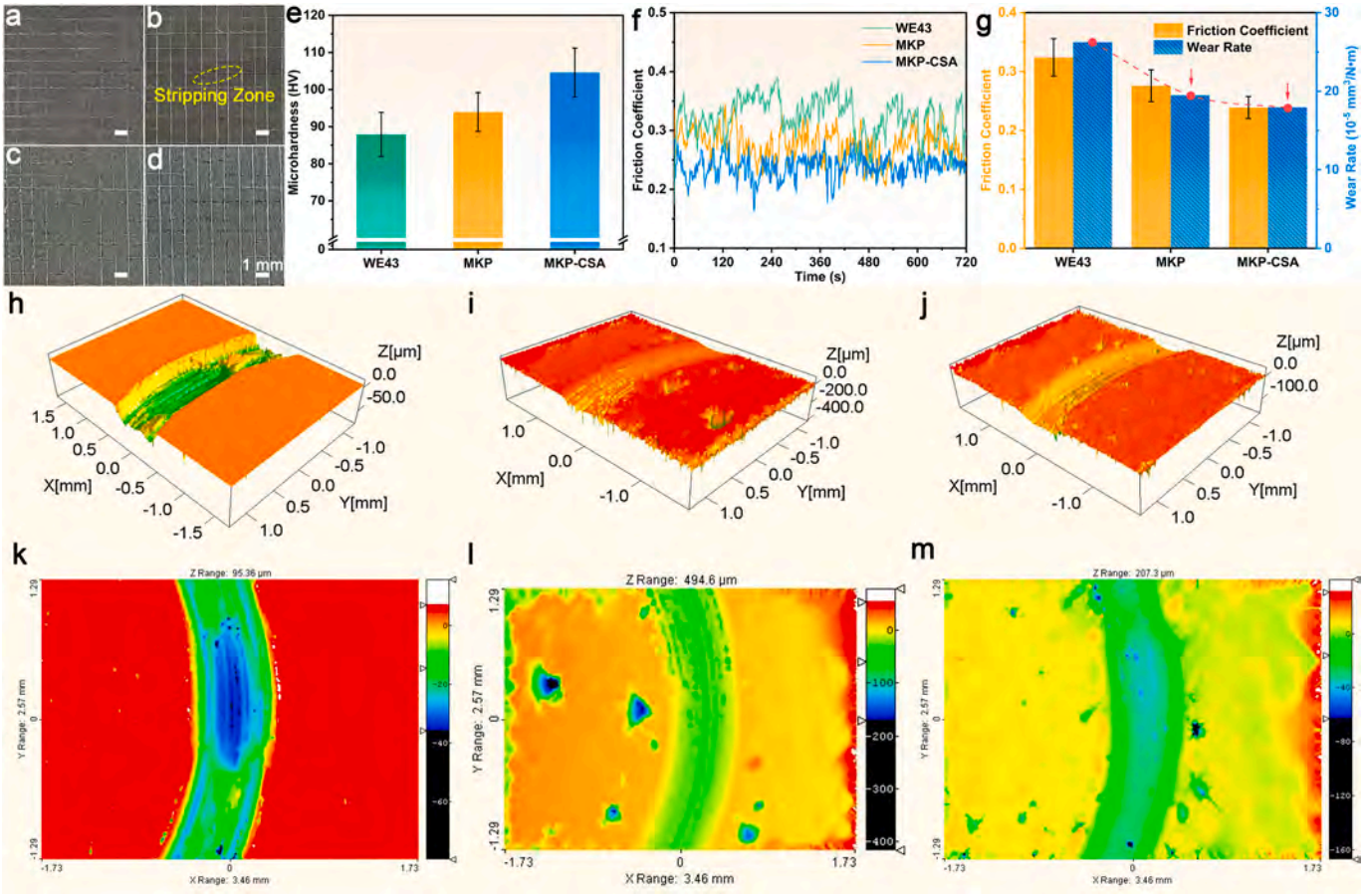

Fig. 10. (a, b) MKP and (c, d) MKP-CSA coatings before and after the cross-cut tape tests; (e) Vickers microhardness values; (f) Friction coefficient curves; (g) Average friction coefficients and wear rates; Wear tracks of (h, k) WE43, (i, l) MKP, and (j, m) MKP-CSA.

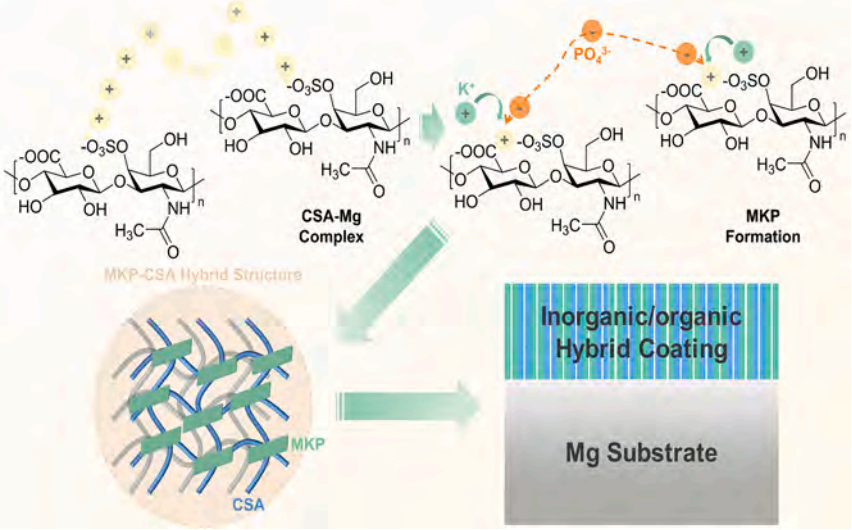

Fig. 11. Schematic diagram showing the formation of the MKP-CSA coating.

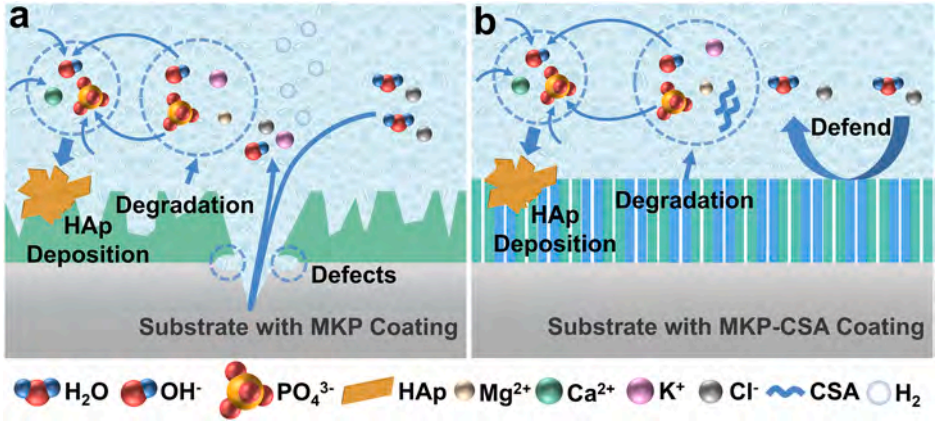

Fig. 12. Corrosion mechanism of the WE43 substrate with MKP/MKP-CSA coating.

products shown in Eqs. (8) and (9) and also releases CSA into the solution. The free CSA reacts with Ca^{2+} to form insoluble Ca–P *in situ*, resulting in spontaneous repair [25,41]. Moreover, CSA aids osteogenesis [22]. As immersion proceeds, due to the close combination of MKP sheets and superior adhesion strength, the hybrid coating does not degrade significantly to provide the necessary corrosion and wear resistance (Fig. 12b).

4.3. Wear mechanism

Orthopedic implants with superior wear resistance can maintain their structural and functional integrity after implantation and avoid unnecessary trouble and trauma for patients. Based on the comparison of the tribological properties of different samples in Fig. 10, the wear resistance is gradually improved in the following orders: WE43 < MKP < MKP-CSA. The wear mechanism is described in Fig. 13. As it is the WE43 Mg alloy (Fig. 13a), during the contact between its surface and friction pair, loss or plastic deformation occurs continuously to change the surface state. The wear modes of the Mg alloy include abrasive, oxidation, and adhesive wear [42]. When the loading is small, it is mainly abrasive wear involving scratches and damage of hard particles on the material surface [43]. During the initial stage of friction, the surface of Mg alloy cracks and exfoliates under the combined action of periodic alternating friction stress and thermal stress. In the intermediate and later stages, abrasion is actually round and blunt, and the Mg surface is highly plastic. After the abrasive slips on the surface, the load plows out the groove, causing plastic deformation on both sides and accumulation. In the subsequent friction process, the accumulated parts are flattened again, so plastic deformation repeats, resulting in the formation of cracks and peeling. Therefore, furrows are observed from the wear track of the WE43 Mg alloy (Fig. 10h, k).

With regard to the Mg alloy with the MKP-CSA coating, a small number of furrows is still observed from the wear track stemming from mainly abrasive wear. As for the MKP coating, the flaky MKP on the surface is crushed to form debris in the initial stage of friction. Subsequently, the abrasive debris is swept across the coating surface, but due to the protective coating, wear is resisted to a certain extent. However, because of the lack of close bonding between layers of MKP, the bonding strength between the inorganic coating and substrate is not high enough, and it can only provide limited wear protection.

CSA chelated with Mg^{2+} during the formation of the hybrid coating provides *in situ* nucleation sites for the formation of MKP. Therefore, the interior of the MKP-CSA coating has strong bonding, and the bonding strength with the substrate is also higher. This undoubtedly plays a key role in resisting further damage to the substrate by abrasive debris. The addition of CSA can reduce the reunion of MKP sheets, and the research shows that less reunion is beneficial to improve the hardness [44]. Higher hardness is also vital for MKP-CSA coating to resist wear. At the same time, the plasticity of CSA itself can also play a certain role in reducing wear, and the combination of hard MKP and soft CSA disperses

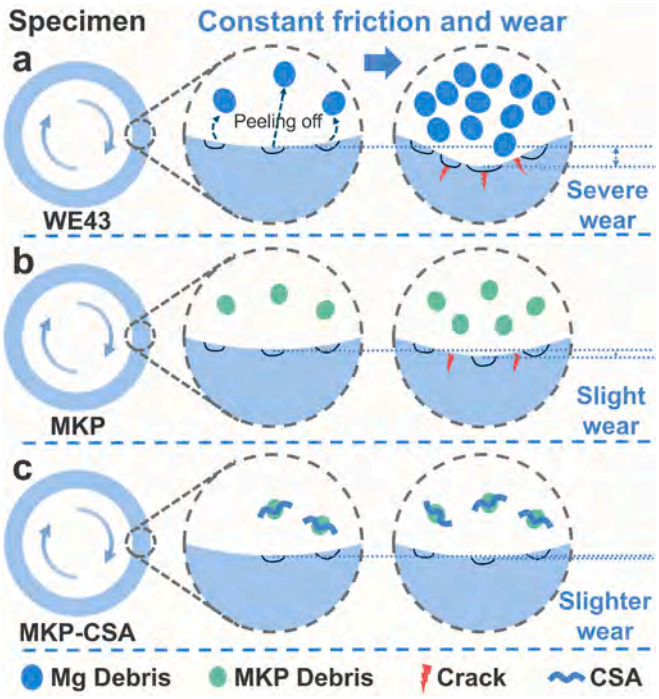

Fig. 13. Wear mechanisms of (a) WE43, (b) MKP coating, and (c) MKP-CSA coating.

friction stress and avoids local coating cracking caused by stress concentration [45,46]. It is worth noting that the mixing of softer polymers with wear debris can also reduce wear [47], which is reflected by the smaller average friction coefficient of the MKP-CSA coating.

4.4. Performance comparison

In Fig. 14, the hybrid CSA-tailored coating effectively improves corrosion and wear performance of Mg substrate compared to traditional protective coatings. Although hydrothermal treatment is a basic surface modification technique, it offers several advantages, including high efficiency, low energy consumption, relatively complete coverage of the substrate, and valid control of the microstructure. The pure inorganic coatings, however, face challenges in achieving good corrosion resistance. CSA can provide *in situ* nucleation sites for MKP, which promotes the production of a more uniform protective layer with better physical barrier effect and is expected to increase biological functionality. In comparison to the friction coefficient of other coatings, MKP-CSA coating has relatively better wear resistance. This improvement can be attributed to the higher adhesion strength and hardness, as well as the combination of the relatively hard inorganic material of MKP and soft polymer of CSA. The promotion of corrosion performance and wear resistance of hybrid coating also proves that adding polymer into inorganic coating is beneficial to design better protective coating on Mg alloys.

To summarize, the MKP-CSA coating prepared through hydrothermal treatment exhibits competitive corrosion performance and wear resistance, however there is still a gap when compared to the best performance recorded. Our research group and other researchers interested in this topic will work together to control hydrothermal treatment conditions (temperature, pH, reaction duration, *etc.*), coating composition (composition optimization of inorganic coating raw materials, crosslinking modification of polymer raw materials, *etc.*), and investigate the deep growth mechanism of the coating.

5. Conclusions

A hybrid inorganic ($MgKPO_4{\cdot}6H_2O$, MKP)-organic (chondroitin sulfate A, CSA) coating with improved corrosion and wear resistance is prepared hydrothermally. The MKP-CSA coating with a more uniform morphology has larger adhesion strength attributable to the ability of CSA to provide stable *in situ* nucleation sites for the formation of MKP. Both the corrosion current density (i_{corr}) and hydrogen evolution rate (HER) of the hybrid coating are one order of magnitude lower than those of the substrate, in addition to the formation of hydroxyapatite (HAp) during immersion. The MKP-CSA coating reduces the average friction coefficient and wear rate from 0.324 ± 0.032 and 26.26×10^{-5} $mm^3/N{\cdot}m$ to 0.239 ± 0.019 and 17.94×10^{-5} $mm^3/N{\cdot}m$, showing superior wear resistance. CSA chelates with Mg^{2+} to form the CSA-Mg complex, which facilitates the stable nucleation of flaky MKP and enhances the adhesion strength as well as the morphology of the hybrid coating. Continuous corrosion protection by the hybrid coating arises from the more uniform and crack-free morphology, and the wear resistance is improved on account of the higher adhesion strength and microhardness, and reasonable collocation of hard MKP with soft CSA. This study reveals a novel strategy to fabricate hybrid inorganic-organic coatings on biodegradable magnesium alloys with outstanding corrosion and wear resistance for clinical practice.

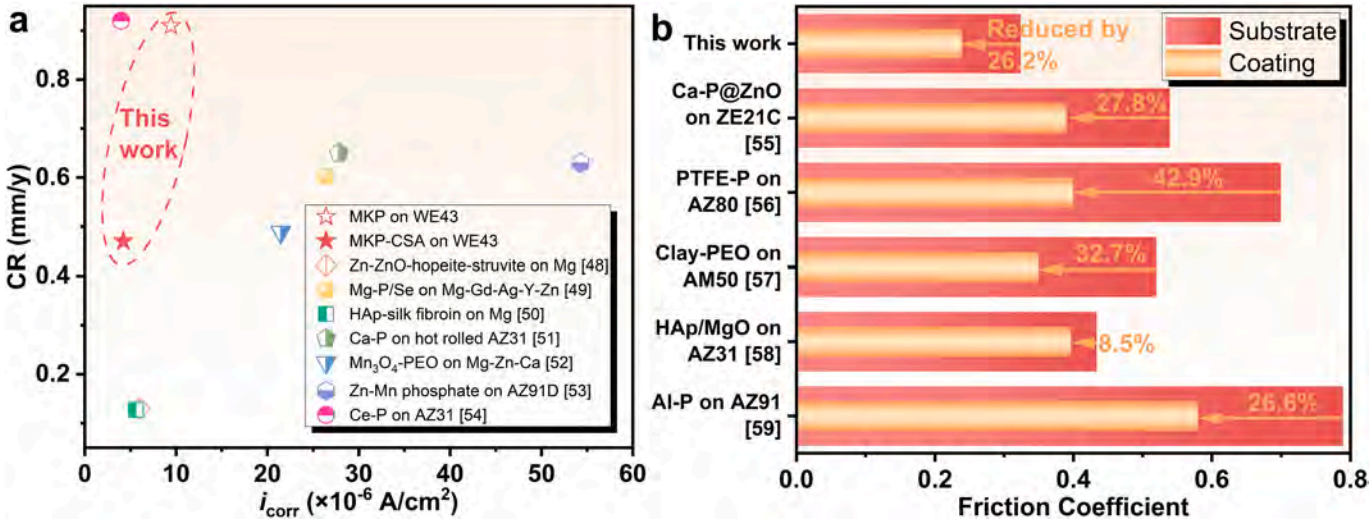

Fig. 14. Comparison of (a) corrosion performance [48–54] and (b) wear resistance [55–59] of different samples.

CRediT authorship contribution statement

Lei Yang: Writing – review & editing, Writing – original draft, Visualization, Formal analysis, Data curation. **Yanbin Zhao:** Writing – original draft, Supervision, Formal analysis. **Yumeng Dong:** Visualization, Software, Formal analysis. **Juyi Yang:** Resources, Formal analysis. **Shuyi Wang:** Visualization. **Cheng Wang:** Investigation. **Jing Bai:** Conceptualization. **Feng Xue:** Project administration. **Paul K. Chu:** Writing – review & editing. **Chenglin Chu:** Writing – review & editing, Writing – original draft, Supervision, Resources, Funding acquisition.

Declaration of competing interest

The authors declare that they have no known competing financial interests or personal relationships that could have appeared to influence the work reported in this paper.

Acknowledgements

This work was supported by the National Natural Science Foundation of China (Grant number 52171236), State Key Program of National Natural Science Foundation of China (Grant number 52231005), Open Research Fund of Jiangsu Key Laboratory for Advanced Metallic Materials, Southeast University (Grant number AMM2024A01), Suzhou Science and Technology Project (Grant numbers SJC2023005, SZS2023023), City University of Hong Kong Strategic Research Grant (SRG) (Grant number 7005505), as well as City University of Hong Kong Donation Research Grant (Grant number DON-RMG 9229021).

Data availability

Data will be made available on request.

References

[1] H.L. Jin, L. Yang, L. Cui, L. Chen, Y.L. Lai, H.M. Guo, Y. Liu, Study on properties of Zn-xMg (x=0.5, 0.8, 1) alloys for potential stent material, J. Mater. Eng. Perform. 32 (16) (2023) 7468–7479.
[2] J.Y. Yang, B.W. Sun, J.W. Dai, X. Li, Y.B. Zhao, L. Zhang, J. Bai, F. Xue, C.L. Chu, Design and fabrication of durable poly(3-hydroxybutyrate) (PHB) coating with high adhesion and desirable anti-corrosion performance on mg alloy for bio-application, Prog. Org. Coat. 194 (2024) 108577.
[3] L. Zhang, X. Zhang, J.W. Dai, J.Y. Yang, J. Bai, Z.H. Huang, C. Guo, F. Xue, L. Y. Han, C.L. Chu, Effects of different magnitudes of static stress on the in vitro corrosion behavior of biodegradable zinc, Corrosion Sci. 227 (2024) 111763.
[4] Y.B. Zhao, P. He, J.Y. Yao, M. Li, B. Wang, L.Y. Han, Z.H. Huang, C. Guo, J. Bai, F. Xue, Y. Cong, W.H. Cai, P.K. Chu, C.L. Chu, pH/NIR-responsive and self-healing coatings with bacteria killing, osteogenesis, and angiogenesis performances on magnesium alloy, Biomaterials 301 (2023) 122237.
[5] L. Yang, Y.L. Lai, K.L. Yue, Y. Liu, H.L. Jin, Corrosion research and fractal characteristics of as-cast and semisolid AZ91D magnesium alloys, Corrosion 79 (7) (2023) 762–770.
[6] H.L. Jin, L. Yang, Y.L. Lai, Y. Liu, The effects of Zr content and hot rolling on the microstructure and mechanical properties of Zn-1.5Cu-1.0Ag-xZr alloys, J. Alloy. Compd. 912 (2022) 165116.
[7] V.K. Bommala, M.G. Krishna, C.I. Rao, Magnesium matrix composites for biomedical applications, J. Magnes. Alloy. 7 (1) (2019) 72–79.
[8] J.W. Dai, J.Y. Yang, X.G. Zhang, L. Zhang, B.W. Sun, X. Li, J. Bai, F. Xue, C.L. Chu, Synergistic effects of BSA adsorption and shear stress on corrosion behaviors of WE43 alloy under simulated physiological flow field, Corrosion Sci. 237 (2024) 112317.
[9] J.G. Zheng, X.Z. Xiao, L.T. Zhang, S.Q. Li, H.W. Ge, L.X. Chen, Facile synthesis of bowl-like 3D $Mg(BH_4)_2$-$NaBH_4$-fluorographene composite with unexpected superior dehydrogenation performances, J. Mater. Chem. A 5 (20) (2017) 9723–9732.
[10] Q.S. Dong, J.H. Jiang, J.H. Zhang, Z. Hu, X.B. Zhang, Clarifying Stress Corrosion Cracking Behavior of Biomedical Mg-Gd-Zn-Zr Alloy, J. Magnes, Alloy, 2024.
[11] X.Y. Yao, J.C. Tang, Y.H. Zhou, A. Atrens, M.S. Dargusch, B. Wiese, T. Ebel, M. Yan, Surface modification of biomedical Mg-Ca and Mg-Zn-Ca alloys using selective laser melting: corrosion behaviour, microhardness and biocompatibility, J. Magnes. Alloy. 9 (6) (2021) 2155–2168.
[12] Y.B. Zhao, J. Bai, F. Xue, R.C. Zeng, G.M. Wang, P.K. Chu, C.L. Chu, Smart self-healing coatings on biomedical magnesium alloys: a review, Smart Materials in Manufacturing 1 (2023) 100022.
[13] L. Ling, S. Cai, Q.Q. Li, J.Y. Sun, X.G. Bao, G.H. Xu, Recent advances in hydrothermal modification of calcium phosphorus coating on magnesium alloy, J. Magnes. Alloy. 10 (1) (2022) 62–80.
[14] E. Babaie, B. Lin, V.K. Goel, S.B. Bhaduri, Evaluation of amorphous magnesium phosphate (AMP) based non-exothermic orthopedic cements, Biomed. Mater. 11 (5) (2016) 055010.
[15] M.H. Esnaashary, A. Khavandi, H.R. Rezaie, J. Javadpour, Mg-P/c-SWCNT bone cement: the effect of filler on setting behavior, compressive strength and biocompatibility, J. Bionic Eng. 17 (1) (2020) 100–112.
[16] M.A. Goldberg, P.A. Krohicheva, A.S. Fomin, D.R. Khairutdinova, O.S. Antonova, A.S. Baikin, V.V. Smirnov, A.A. Fomina, A.V. Leonov, I.V. Mikheev, N.S. Sergeeva, S.A. Akhmedova, S.M. Barinov, V.S. Komlev, In situ magnesium calcium phosphate cements formation: from one pot powders precursors synthesis to in vitro investigations, Bioact. Mater. 5 (3) (2020) 644–658.
[17] S.L. Tan, Y.F. Wang, Y.Y. Du, Y. Xiao, S.M. Zhang, Injectable bone cement with magnesium-containing microspheres enhances osteogenesis via anti-inflammatory immunoregulation, Bioact. Mater. 6 (10) (2021) 3411–3423.
[18] R. Shishir, E. Lokeshkumar, P. Manojkumar, U. Nasiruddin, C. Premchand, V. Ponnilavan, L.R. Krishna, N. Rameshbabu, Development of biocompatible and corrosion-resistant plasma electrolytic oxidation coating over zinc for orthopedic implant applications, Surf. Coat. Technol. 450 (2022) 128990.
[19] J. Wang, Z.C. Wang, J.H. Dou, Y.K. Li, C. Hu, H.J. Yu, C.Z. Chen, Effect of potassium fluotitanate concentration on the corrosion resistance and degradation property of micro-arc oxidized ZM21 magnesium alloys, J. Mater. Res. Technol-JMRT 25 (2023) 2527–2544.
[20] Y.F. Ren, E. Babaie, S.B. Bhaduri, Nanostructured amorphous magnesium phosphate/poly (lactic acid) composite coating for enhanced corrosion resistance and bioactivity of biodegradable AZ31 magnesium alloy, Prog. Org. Coat. 118 (2018) 1–8.
[21] Y.B. Zhao, Y.Y. Li, B. Wang, J.Y. Yao, Y. Fan, P. He, J. Bai, C. Wang, F. Xue, C. L. Chu, An injectable magnesium-based cement stimulated with NIR for drug-controlled release and osteogenic potential, Adv. Healthc. Mater. 13 (19) (2024) 2400207.
[22] Q.S. Shen, Y.J. Guo, K.Y. Wang, C.H. Zhang, Y.L. Ma, A review of chondroitin sulfate's preparation, properties, functions, and applications, Molecules 28 (20) (2023) 7093.
[23] Y.Z. Wu, Z.C. Lyu, F. Hu, L.J. Yang, K. Yang, M. Chen, Y. Wang, A chondroitin sulphate hydrogel with sustained release of SDF-1α for extensive cartilage defect repair through induction of cell homing and promotion of chondrogenesis, J. Mat. Chem. B 12 (35) (2024) 8672–8687.
[24] L. Zhou, L. Fan, F.M. Zhang, Y.H. Jiang, M. Cai, C. Dai, Y.A. Luo, L.J. Tu, Z.N. Zhou, X.J. Li, C.Y. Ning, K. Zheng, A.R. Boccaccini, G.X. Tan, Hybrid gelatin/oxidized chondroitin sulfate hydrogels incorporating bioactive glass nanoparticles with enhanced mechanical properties, mineralization, and osteogenic differentiation, Bioact. Mater. 6 (3) (2021) 890–904.
[25] H.D. Kim, E.A. Lee, Y.H. An, S.L. Kim, S.S. Lee, S.J. Yu, H.L. Jang, K.T. Nam, S. G. Im, N.S. Hwang, Chondroitin sulfate-based biomineralizing surface hydrogels for bone tissue engineering, ACS Appl. Mater. Interfaces 9 (26) (2017) 21639–21650.
[26] M. Al-Amin, A.M. Abdul-Rani, M. Danish, S. Rubaiee, A. bin Mahfouz, H. M. Thompson, S. Ali, D.R. Unune, M.H. Sulaiman, Investigation of coatings, corrosion and wear characteristics of machined biomaterials through hydroxyapatite mixed-EDM process, A Review, Materials 14 (13) (2021) 3597.
[27] N. Murugan, C. Murugan, A.K. Sundramoorthy, In vitro and in vivo characterization of mineralized hydroxyapatite/polycaprolactone-graphene oxide based bioactive multifunctional coating on Ti alloy for bone implant applications, Arab. J. Chem. 11 (6) (2018) 959–969.
[28] J.M. Zhang, A.R. Hou, J.C. Li, D.D. Lian, M.C. Zhang, Z.H. Wang, Enhanced corrosion and wear resistance of LA43M magnesium-lithium alloy with magnesium-aluminum layered double hydroxide coating, J. Mater. Eng. Perform. 32 (8) (2023) 3550–3562.
[29] J.Y. Yang, Y.B. Zhao, J.W. Dai, L.Y. Han, Q.S. Dong, L. Zhang, J. Bai, F. Xue, P. K. Chu, C.L. Chu, Fabrication and growth mechanism of multilayered hydroxyapatite/organic composite coatings on the WE43 magnesium alloy, Surf. Coat. Technol. 452 (2023) 129125.
[30] Y.B. Zhao, X.Y. Chen, S.Q. Li, R.C. Zeng, F. Zhang, Z.L. Wang, S.K. Guan, Corrosion resistance and drug release profile of gentamicin-loaded polyelectrolyte multilayers on magnesium alloys: effects of heat treatment, J. Colloid. Interf. Sci. 547 (2019) 309–317.
[31] Y.B. Zhao, P. He, B. Wang, J. Bai, F. Xue, C.L. Chu, Incorporating pH/NIR responsive nanocontainers into a smart self-healing coating for a magnesium alloy with controlled drug release, bacteria killing and osteogenesis properties, Acta Biomater. 174 (2024) 463–481.
[32] L. Zhang, X. Zhang, J.E. Chen, J.W. Dai, J. Bai, Z.H. Huang, C. Guo, F. Xue, L. Y. Han, C.L. Chu, Effects of different concentrations of BSA on in vitro corrosion behavior of pure zinc in artificial plasma, ACS Biomater Sci. Eng. 8 (10) (2022) 4365–4376.
[33] Y.B. Zhao, P. He, J.Y. Yao, M. Li, J. Bai, F. Xue, C.L. Chu, Y. Cong, P.K. Chu, Self-assembled multilayered coatings with multiple cyclic self-healing capability, Bacteria killing, osteogenesis, and angiogenesis properties on magnesium alloys, Adv. Healthc. Mater. 13 (9) (2024) e2302519.
[34] L.H. Jiang, M.M. Han, J.J. Sun, M.T. Gong, Y.F. Lin, T. Xiao, P. Xiang, W.F. Chen, X.Y. Tan, Strong mechanical and durable superhydrophobic photothermal MWCNTs/SiO_2/PDMS/PVDF composite coating for anti-icing and de-icing, Prog. Org. Coat. 174 (2023) 107282.

[35] X.B. Bai, Q. Cai, C.Q. Dang, J.L. Li, Microstructure and high-temperature tribological properties of TiSiN-Ag coatings deposited by multi-arc ion plating, J. Mater. Sci. 57 (35) (2022) 16892–16903.
[36] D.J. Miller, M.C. Biesinger, N.S. McIntyre, Interactions of CO_2 and CO at fractional atmosphere pressures with iron and iron oxide surfaces: one possible mechanism for surface contamination, Surf. Interface Anal. 33 (4) (2002) 299–305.
[37] L.Y. Li, L.Y. Cui, B. Liu, R.C. Zeng, X.B. Chen, S.Q. Li, Z.L. Wang, E.H. Han, Corrosion resistance of glucose-induced hydrothermal calcium phosphate coating on pure magnesium, Appl. Surf. Sci. 465 (2019) 1066–1077.
[38] M.M. Zhu, J.Y. Yu, Z.L. Li, B. Ding, Self-healing fibrous membranes, Angew. Chem. Int. Ed. 61 (41) (2022) e202208949.
[39] Y.X. Bai, Z.J. Wang, X.L. He, Y.J. Zhu, X. Xu, H.Y. Yang, G.Y. Mei, S.G. Chen, B. Ma, R.R. Zhu, Application of bioactive materials for osteogenic function in bone tissue engineering, Small Methods 8 (8) (2024) 2301283.
[40] X. Mi, M.J. Gupte, Z.P. Zhang, W.B. Swanson, L.K. McCauley, P.X. Ma, Three-dimensional electrodeposition of calcium phosphates on porous nanofibrous scaffolds and their controlled release of calcium for bone regeneration, ACS Appl. Mater. Interfaces 12 (29) (2020) 32503–32513.
[41] J.W. Dai, C.Q. Wu, J.Y. Yang, L. Zhang, Q.S. Dong, L.Y. Han, X. Li, J. Bai, F. Xue, P. K. Chu, C.L. Chu, Poly-lactic acid coatings on the biomedical WE43 Mg alloy: protection mechanism and ion permeation effects, Prog. Org. Coat. 177 (2023) 107427.
[42] J. An, Y.X. Tian, C.Q. Feng, Correlation between test temperature, applied load and wear transition of Mg97Zn1Y2 alloy, J. Magnes. Alloy. 9 (2) (2021) 592–603.
[43] J.Y. Zhang, Y.X. Jian, X.Z. Zhao, D.A. Meng, F.S. Pan, Q.Y. Han, The tribological behavior of a surface-nanocrystallized magnesium alloy AZ31 sheet after ultrasonic shot peening treatment, J. Magnes. Alloy. 9 (4) (2021) 1187–1200.
[44] H. Ahmadian, T.F. Zhou, A. Alansari, A.S. Kumar, A. Fathy, M. Elmahdy, Q. Yu, G. Weijia, Microstructure, mechanical properties and wear behavior of Mg matrix composites reinforced with Ti and nano SiC particles, J. Mater. Res. Technol-JMRT 31 (2024) 4088–4103.
[45] S.W. Chen, Q.Q. Chen, B.G. Wang, H.S. Lu, Carbon dots grafted by oil-soluble polymer brushes derived from bis-alkyl chain monomers as a lubricant additive of poly-α-olefin with outstanding friction-reducing, anti-wear and anti-rust properties, Colloid Surf. A-Physicochem. Eng. Asp. 704 (2025) 135392.
[46] U.O. Uyor, A.P.I. Popoola, O.M. Popoola, Chemically functionalized graphene-boron nitride/polypropylene nanocomposites with enhanced nanomechanical and anti-wear properties, Chem. Afr. J. Tunisian Chem. Soc. 7 (3) (2024) 1595–1604.
[47] Y.B. Zhang, K.M. Yang, R. Liu, J.Y. Yao, H.X. Yan, Superior tough, highly wear durable and self-lubricating epoxy composite co-enhanced by soft and hard nanomaterials, Chem. Eng. J. 460 (2023) 141773.
[48] P.M. Sathyaraj, T. Balusamy, T. Narayanan, K. Ravichandran, Imparting a better corrosion resistance and bioactivity for magnesium through the formation of zinc - zinc oxide - zinc phosphate (hopeite) - magnesium ammonium phosphate (struvite) composite coatings, J. Alloy. Compd. 1002 (2024) 175342.
[49] Y. Zhang, Y. Liu, R.N. Zheng, Microstructure characteristics and degradation behaviors of se/phosphate conversion coatings on Mg-Gd-Ag-Y-Zn alloys in the Hank's electrolyte, Surf. Coat. Technol. 477 (2024) 130387.
[50] M.M. Rahman, R. Balu, A. Abraham, N.K. Dutta, N.R. Choudhury, Engineering a bioactive hybrid coating for in vitro corrosion control of magnesium and its alloy, ACS Appl. Bio Mater. 4 (7) (2021) 5542–5555.
[51] H. Aghamohammadi, S.M. Rabiee, S.J. Hosseinipour, R. Jamaati, Effect of microstructure and texture of AZ31 magnesium alloy substrate on nucleation and growth of biomimetic calcium phosphate coating, J. Mater. Res. Technol-JMRT 27 (2023) 5154–5164.
[52] S. Bahrampour, A. Bordbar-Khiabani, M.H. Siadati, M. Gasik, M. Mozafari, Improving the inflammatory-associated corrosion behavior of magnesium alloys by Mn_3O_4 incorporated plasma electrolytic oxidation coatings, Chem. Eng. J. 483 (2024) 149016.
[53] T.L. Nguyen, T.C. Cheng, J.Y. Yang, C.J. Pan, T.H. Lin, A zinc-manganese composite phosphate conversion coating for corrosion protection of AZ91D alloy: growth and characteristics, J. Mater. Res. Technol-JMRT 19 (2022) 2965–2980.
[54] J. Jayaraj, A. Srinivasan, C. Arunchandran, V. Rajinikanth, Corrosion and in vitro characteristics of cerium phosphate based chemical conversion coating on AZ31 magnesium alloy, Appl. Surf. Sci. 644 (2024) 158797.
[55] X. Li, J.Y. Zhao, D. Mei, J.G. Li, S.J. Yu, F. Liang, X.Y. Wang, L.G. Wang, S.J. Zhu, S. K. Guan, A ZnO and calcium phosphate co-deposited coating on magnesium alloy for better antibacterial property, cytocompatibility and corrosion resistance, Colloid Surf. A-Physicochem. Eng. Asp. 706 (2025) 135834.
[56] E. Mortezanejad, M. Atapour, H. Salimijazi, A. Alhaji, A. Hakimizad, Wear and corrosion behavior of aluminate- and phosphate-based plasma electrolytic oxidation coatings with polytetrafluoroethylene nanoparticles on AZ80 Mg alloy, J. Mater. Eng. Perform. 30 (6) (2021) 4030–4044.
[57] F. Davoodi, M. Atapour, C. Blawert, M. Zheludkevich, Wear and corrosion behavior of clay containing coating on AM 50 magnesium alloy produced by aluminate-based plasma electrolytic oxidation, Trans. Nonferrous Met. Soc. China 31 (12) (2021) 3719–3738.
[58] H. Mozafarnia, A. Fattah-Alhosseini, R. Chaharmahali, M. Nouri, M.K. Keshavarz, M. Kaseem, Corrosion, Wear, and antibacterial behaviors of hydroxyapatite/MgO composite PEO coatings on AZ31 Mg alloy by incorporation of TiO_2 nanoparticles, Coatings 12 (12) (2022) 1967.
[59] E. Selvi, M. Kaba, F. Muhaffel, A.S. Vanli, M. Baydogan, Elevated temperature wear behavior of AZ91 magnesium alloy after micro-arc oxidation in single and dual phase electrolytes, J. Tribol.-Trans. ASME 145 (7) (2023) 071701.

Surface & Coatings Technology 505 (2025) 132103

Contents lists available at ScienceDirect

Surface & Coatings Technology

journal homepage: www.elsevier.com/locate/surfcoat

Corrigendum

Corrigendum to "Hybrid chondroitin sulfate-tailored phosphate coatings for improved corrosion and wear resistance of WE43 magnesium alloy" [Surf. Coat. Technol. 503 (2025) 132012]

Lei Yang [a,b], Yanbin Zhao [a,b,d], Yumeng Dong [a,b], Juyi Yang [a,b], Shuyi Wang [a,b], Cheng Wang [a,b], Jing Bai [a,b,c], Feng Xue [a,b], Paul K. Chu [d], Chenglin Chu [a,b,*]

[a] School of Materials Science and Engineering, Southeast University, Nanjing 211189, China
[b] Jiangsu Key Laboratory for Advanced Metallic Materials, Southeast University, Nanjing 211189, China
[c] Institute of Medical Devices (Suzhou), Southeast University, Suzhou 215163, China
[d] Department of Physics, Department of Materials Science and Engineering, and Department of Biomedical Engineering, City University of Hong Kong, Hong Kong, China

We regret "the electrochemical curves of MKP sample with slightly different experimental parameters in the early exploration process were carelessly applied in Fig. 5, so some related data and statements are corrected this time". This oversight does not affect the novelty and conclusion of the article.

(1) Correction to "the electrochemical curves of MKP sample". Due to our negligence in proofreading, in this article, a correction on the yellow line of Fig. 5(a–d).

(2) Correction to "E_{corr} and i_{corr} determined from the potentiodynamic polarization curves". In this article, a correction on Table 1.

(3) Correction to "Fitted electrochemical parameters by EIS simulation". In this article, a correction on Table 2.

(4) Correction to "Since E_{corr} (WE43 (- 1.743 V/SCE) < MKP (- 1.679 V/SCE) < MKP-CSA (- 1.532 V/SCE)), the MKP-CSA coating enhances the thermodynamic stability during corrosion", "The i_{corr} values of both coatings (9.576×10^{-6} and 4.219×10^{-6} A/cm^2) are one order of magnitude less than that of the substrate (2.489×10^{-5} A/cm^2)", and "By applying the MKP coating, R_{ct} increases from 210.90 to 1172.00 Ω·cm^2, while the hybrid coating reaches 1736.13 Ω·cm^2". In this article, a correction on Sec. 3.2.

We hope to adhere to the journal's correction policy to amend the above error to uphold academic integrity and the reliability of the research. We would like to apologise for any inconvenience caused.

DOI of original article: https://doi.org/10.1016/j.surfcoat.2025.132012.
* Corresponding author at: School of Materials Science and Engineering, Southeast University, Nanjing 211189, China.
E-mail address: clchu@seu.edu.cn (C. Chu).

https://doi.org/10.1016/j.surfcoat.2025.132103

Available online 2 April 2025
0257-8972/© 2025 Elsevier B.V. All rights are reserved, including those for text and data mining, AI training, and similar technologies.

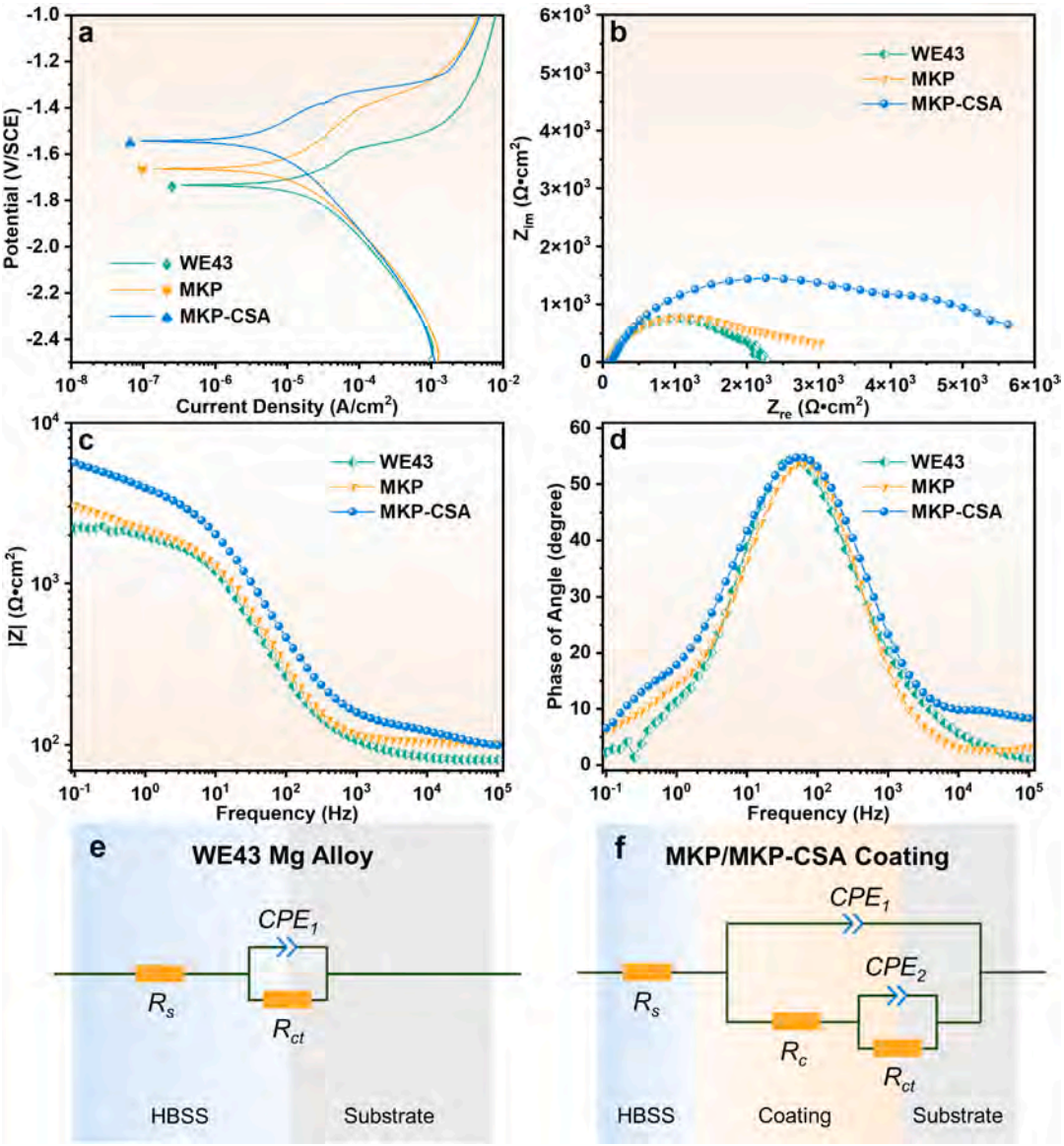

Fig. 5. Electrochemical properties of the Mg substrate, MKP and MKP-CSA coatings: (a) Potentiodynamic polarization curves; (b) Impedance spectra; (c) Bode plots; (d) Bode plots of phase angle vs. frequency; Equivalent circuits for (e) substrate and (f) coatings.

Table 1
E_{corr} and i_{corr} determined from the potentiodynamic polarization curves.

Samples	E_{corr} (V/SCE)	i_{corr} (A/cm^2)
WE43	−1.743	2.489×10^{-5}
MKP	−1.679	9.576×10^{-6}
MKP-CSA	−1.532	4.219×10^{-6}

Table 2
Fitted electrochemical parameters by EIS simulation.

Samples	WE43	MKP	MKP-CSA
R_s (Ω·cm^2)	82.75	103.00	112.5
CPE_1 (Ω^{-1}·cm^{-2}·s^{-1})	2.38×10^{-5}	1.39×10^{-5}	1.66×10^{-5}
n_1	0.80	0.87	0.77
R_c (Ω·cm^2)	–	1832.00	4344.00
CPE_2 (Ω^{-1}·cm^{-2}·s^{-1})	–	4.01×10^{-4}	3.91×10^{-4}
n_2	–	0.72	0.93
R_{ct} (Ω·cm^2)	210.90	1172.00	1736.13
χ^2	1.62×10^{-3}	4.49×10^{-4}	4.91×10^{-3}

(*continued on next column*)

Table 2 (*continued*)

(*continued from previous column*)

Declaration of competing interest

The authors declare that they have no known competing financial interests or personal relationships that could have appeared to influence the work reported in this paper.

Data availability

Data will be made available on request.